

CARMA LARGE AREA STAR FORMATION SURVEY: DENSE GAS IN THE YOUNG L1451 REGION OF PERSEUS

Shaye Storm^{1,2}, Lee G. Mundy², Katherine I. Lee^{1,2}, Manuel Fernández-López^{3,4}, Leslie W. Looney³, Peter Teuben², Héctor G. Arce⁵, Erik W. Rosolowsky⁶, Aaron M. Meisner⁷, Andrea Isella⁸, Jens Kauffmann⁹, Yancy L. Shirley¹⁰, Woojin Kwon¹¹, Adele L. Plunkett¹², Marc W. Pound², Dominique M. Segura-Cox³, Konstantinos Tassis^{13,14}, John J. Tobin¹⁵, Nikolaus H. Volgenau¹⁶, Richard M. Crutcher³, Leonardo Testi¹⁷

Accepted to The Astrophysical Journal (ApJ); June 25, 2016

(see published version for full-resolution figures)

ABSTRACT

We present a 3 mm spectral line and continuum survey of L1451 in the Perseus Molecular Cloud. These observations are from the CARMA Large Area Star Formation Survey (CLASSy), which also imaged Barnard 1, NGC 1333, Serpens Main and Serpens South. L1451 is the survey region with the lowest level of star formation activity—it contains no confirmed protostars. HCO⁺, HCN, and N₂H⁺ ($J = 1 \rightarrow 0$) are all detected throughout the region, with HCO⁺ the most spatially widespread, and molecular emission seen toward 90% of the area above N(H₂) column densities of $1.9 \times 10^{21} \text{ cm}^{-2}$. HCO⁺ has the broadest velocity dispersion, near 0.3 km s^{-1} on average, compared to $\sim 0.15 \text{ km s}^{-1}$ for the other molecules, thus representing a range from supersonic to subsonic gas motions. Our non-binary dendrogram analysis reveals that the dense gas traced by each molecule has similar hierarchical structure, and that gas surrounding the candidate first hydrostatic core (FHSC), L1451-mm, and other previously detected single-dish continuum clumps have similar hierarchical structure; this suggests that different sub-regions of L1451 are fragmenting on the pathway to forming young stars. We determined the three-dimensional morphology of the largest detectable

¹Harvard-Smithsonian Center for Astrophysics, 60 Garden Street, Cambridge, MA 02138, USA

²Department of Astronomy, University of Maryland, College Park, MD 20742, USA; sstorm@astro.umd.edu

³Department of Astronomy, University of Illinois at Urbana–Champaign, 1002 West Green Street, Urbana, IL 61801, USA

⁴Instituto Argentino de Radioastronomía, CCT-La Plata (CONICET), C.C.5, 1894, Villa Elisa, Argentina

⁵Department of Astronomy, Yale University, P.O. Box 208101, New Haven, CT 06520-8101, USA

⁶University of Alberta, Department of Physics, 4-181 CCIS, Edmonton AB T6G 2E1, Canada

⁷Lawrence Berkeley National Laboratory and Berkeley Center for Cosmological Physics, Berkeley, CA 94720, USA

⁸Physics & Astronomy Department, Rice University, P.O. Box 1892, Houston, TX 77251-1892, USA

⁹Max Planck Institut für Radioastronomie, Auf dem Hügel 69 D53121, Bonn Germany

¹⁰Steward Observatory, 933 North Cherry Avenue, Tucson, AZ 85721, USA

¹¹Korea Astronomy and Space Science Institute, 776 Daedeok-daero, Yuseong-gu, Daejeon 305-348, Republic of Korea

¹²European Southern Observatory, Av. Alonso de Cordova 3107, Vitacura, Santiago de Chile

¹³Department of Physics and Institute of Theoretical & Computational Physics, University of Crete, PO Box 2208, GR-710 03, Heraklion, Crete, Greece

¹⁴Foundation for Research and Technology - Hellas, IESL, Voutes, 7110 Heraklion, Greece

¹⁵Leiden Observatory, 540 J.H. Oort Building, Niels Bohrweg 2, NL-2333 CA Leiden, The Netherlands

¹⁶Las Cumbres Observatory Global Telescope Network, Inc. 6740 Cortona Drive, Suite 102 Goleta, CA 93117, USA

¹⁷ESO, Karl-Schwarzschild-Strasse 2 D-85748 Garching bei München, Germany

dense gas structures to be relatively ellipsoidal compared to other CLASSy regions, which appeared more flattened at largest scales. A virial analysis shows the most centrally condensed dust structures are likely unstable against collapse. Additionally, we identify a new spherical, centrally condensed N_2H^+ feature that could be a new FHSC candidate. The overall results suggest L1451 is a young region starting to form its generation of stars within turbulent, hierarchical structures.

1. Introduction

The star formation process in a molecular cloud starts well before protostars are detectable at infrared wavelengths. In general, it begins with the formation of the molecular cloud that may span tens of parsecs (Evans 1999; Elmegreen & Scalo 2004; McKee & Ostriker 2007); it continues as structure and density enhancements are created by the interaction of turbulence, gravity, and magnetic fields at parsec scales (McKee & Ostriker 2007; Crutcher 2012), and it progresses until prestellar core collapse occurs at 0.01–0.1 pc scales (di Francesco et al. 2007; Bergin & Tafalla 2007). Once a first generation of protostars is formed within those dense cores, the young stars can feed energy back into the cloud and impact subsequent star formation that may occur (Nakamura & Li 2007; Carroll et al. 2009; Nakamura & Li 2014). A full understanding of how turbulence, gravity, and magnetic fields control the star formation process requires observations that span cloud to core spatial scales at these distinct evolutionary stages.

An individual molecular cloud can be a great testbed for studying the star formation process across space and time if it is sufficiently close to get better than 0.1 pc resolution, and if it contains regions with distinct evolutionary stages. The Perseus Molecular Cloud is a nearby example of such a cloud. The regions of Perseus with infrared detections of young stellar objects (YSOs) span a range of evolutionary epochs based on YSO statistics from the c2d Legacy project (Jørgensen et al. 2008; Evans et al. 2009). For example, the IC 348 region has 121 YSOs, with 9.1% being Class I or younger; the NGC 1333 region has 102 YSOs, with 34% being Class I or younger; Barnard 1 region has 9 YSOs, with 89% being Class I or younger. Regions without current protostellar activity also exist within Perseus. The B1-E region may be forming a first generation of dense cores (Sadavoy et al. 2012), and the L1451 region has a single detection of a compact continuum core, which is a candidate first hydrostatic core (FHSC) (Pineda et al. 2011).

The CARMA Large Area Star Formation Survey (CLASSy) observed the dense gas in three evolutionary distinct regions within Perseus (Storm et al. 2014) and two regions within Serpens (Lee et al. 2014; Fernández-López et al. 2014) with high angular and velocity resolution. The observations enable a high resolution study of the structure and kinematics of star forming material at different epochs. From early to late stages of evolution (based on the ratio of Class II and older to Class I and younger YSOs), the Perseus regions of CLASSy are L1451, Barnard 1, and NGC 1333. The youngest region, L1451, probes cloud conditions during the origin of clumps and stars; the more evolved Barnard 1 region probes cloud conditions when a relatively small number of protostars are formed, and the active NGC 1333 region probes cloud conditions when dozens of clustered protostars are driving outflows back into the cloud. Details of CLASSy, along with an analysis of Barnard 1, can be found in Storm et al. (2014) (referred to as Paper I in the sections below).

This paper focuses on the L1451 region. L1451 is located ~ 5.5 pc to the southwest of NGC 1333 (see Figure 1 of Paper I). The region has been surveyed at a number of wavelengths as reported in the literature and summarized below. It contains no *Spitzer*-identified YSOs at IRAC or MIPS wavelengths (Jørgensen et al. 2008)¹. Hatchell et al. (2005) and Kirk et al. (2006) did not identify any cores in their JCMT SCUBA 850 μm survey. There are four 1.1 mm sources identified in the Bolocam Survey (Enoch et al. 2006) that are classified as “starless” cores in Enoch et al. (2008): PerBolo 1, 2, 4, and 6. Pineda et al. (2011) used 3 mm CARMA and

¹The *Spitzer* c2d YSO sample is 90% complete down to $0.05 L_\odot$ for clouds at 260 pc (Evans et al. 2009).

1.3 mm SMA observations to show that PerBolo 2 is not a starless core, but likely a core with an embedded YSO or a FHSC.

The Bolocam cores within L1451 are colder and less dense than the average Bolocam cores within Perseus. The visual extinction (A_V) of the four Bolocam sources ranges from 8 to 11 magnitudes, while the mean and median A_V for all Perseus sources are 24.6 and 12, respectively (Enoch et al. 2006). The mean particle density of the L1451 Bolocam sources ranges from 0.9×10^5 to 1.5×10^5 cm^{-3} , which is lower than the mean density for all Perseus sources of 3.2×10^5 (Enoch et al. 2008). The kinetic temperature of gas within the L1451 cores ranges from 9.1 to 10.3 K, which is lower than the mean for all Perseus cores of 11.0 (Rosolowsky et al. 2008a). These statistics complement the YSO statistics that suggest L1451 it is at an earlier evolutionary epoch than Barnard 1 and NGC 1333.

The main science goals of our large-area, high-resolution, spectral line observations of this young region are: 1) to quantify the dense gas content of a cloud region possibly at the onset of star formation, 2) to determine whether complex, hierarchical structure formation exists before the onset of star formation, as predicted by theories of turbulence-driven star formation, 3) to better understand how natal cloud material fragments on the pathway to star formation, by quantifying the hierarchical similarities and differences between sub-regions of L1451 with and without compact cores, 4) to estimate the boundedness of the dense structures in young star forming regions, and 5) to potentially discover new young cores.

The paper is organized as follows. Section 2 provides an overview of CLASSy observations of L1451. Properties of the L1451-mm continuum detection are in Section 3. Section 4 presents the dense gas morphology using integrated intensity and channel maps, and Section 5 presents the dense gas kinematic results from spectral line fitting. A dendrogram analysis of the HCO^+ , HCN , and N_2H^+ data cubes is in Section 6. Section 7 shows how we calculate column density, dust temperature, and extinction maps using *Herschel* data, along with a dendrogram analysis of the extinction map. Section 8 discusses the current state of star formation in L1451 using the spectral line data in combination with the continuum data to further quantify physical and spatial properties of structures in L1451. We summarize our key findings in Section 9.

2. Observations

The details of CLASSy observations, calibration, and mapping are found in Paper I; specifics related to L1451 are summarized here. We mosaicked a total area of ~ 150 square arcminutes in CARMA23 mode, which uses all 23 CARMA antennas. The mosaic was made up of two adjacent rectangles, containing a total of 673 individual pointings with $31''$ spacing in a hexagonal grid (see Figure 1). The reference position of the mosaic is at the center of the eastern rectangle: $\alpha=03^{\text{h}}25^{\text{m}}17^{\text{s}}$, $\delta=30^{\circ}21'23''$ (J2000). The L1451-mm core (Pineda et al. 2011) is within the eastern rectangle. The region was observed for 150 total hours, split between the DZ and EZ configurations, which provide projected baselines from about 1–40 k λ and 1–30 k λ , respectively, and a hybrid array (DEZ) with baselines ranging from about 1–35 k λ . The DEZ array was not used for the CLASSy observations presented in Paper I, and is the reason the synthesized beam for L1451 is slightly larger than that for Barnard 1. See Table 1 for a summary of observing dates and calibrators. The mapped region covers roughly 1.1 pc by 0.6 pc with about 1800 AU spatial resolution.

The correlator setup is summarized in Table 2. N_2H^+ , HCO^+ , and HCN ($J = 1 \rightarrow 0$) were simultaneously observed in 8 MHz bands, providing a velocity resolution of 0.16 km s^{-1} . We also used a 500 MHz band for continuum observations and calibration. Data were inspected and calibrated using MIRIAD (Multichannel Image Reconstruction, Image Analysis and Display; Sault et al. 1995) as described in Paper I. 3C84 was observed every 16 minutes for gain calibration; 3C111 was used for gain calibration when 3C84 transited above 80 degrees elevation. Uranus was observed for absolute flux calibration. The flux of 3C84 varied between 16 and 21 Jy over the observing period, while 3C111 varied between 2.6 and 4.5 Jy. The uncertainty in absolute flux calibration

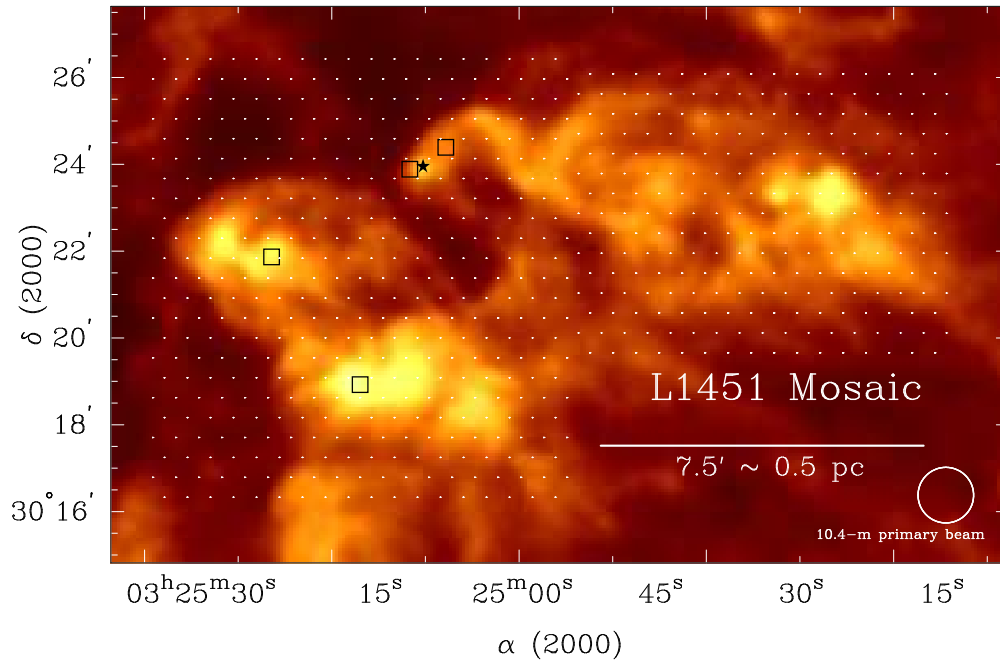


Fig. 1.— A *Herschel* image of the $250\ \mu\text{m}$ emission (yellow is brighter emission, red is fainter emission) from L1451 with the CLASSy mosaic pointing centers overlaid as white points. The spacing of the pointing centers is $31''$, and our total area coverage is ~ 150 square arcminutes. The locations of 1.1 mm Bolocam sources (Enoch et al. 2006) and the L1451-mm compact continuum core (Pineda et al. 2011) are marked with black squares and a black star, respectively.

is about 10%. We will only report statistical uncertainties when quoting errors in measured values throughout the paper.

To create spectral-line images which fully recover emission at all spatial scales, CARMA observed in single-dish mode during tracks with stable atmospheric opacity. The OFF position for L1451 was $3.5'$ west and $13.7'$ south of the mosaic reference position, at the location of a gap in ^{12}CO and ^{13}CO emission to ensure no significant dense gas contribution. The single-dish data from the 10.4-m dishes was calibrated in MIRIAD as described in Paper I. The antenna temperature rms in the final single-dish cubes was ~ 0.02 K for all three molecules. The spectral-line interferometric and single-dish data were combined with *mosmem*, a maximum entropy joint deconvolution algorithm in MIRIAD. The noise levels and synthesized beams for the final data cubes are given in Table 2. The rms noise in these lines correspond to brightness temperature rms of 0.34 K for N_2H^+ and 0.30 K for HCO^+ and HCN.

We created a 3 mm continuum map with the interferometric data from the 500 MHz window. The rms in the continuum map is ~ 1.3 mJy beam $^{-1}$ with a synthesized beam of $9.2'' \times 6.6''$. Single-dish continuum data can not be acquired at CARMA.

Table 1. Observation Summary

Array	Dates	Total Hours	Flux Cal.	Gain Cal.	Mean Flux (Jy)
DZ	October 2012	25	Uranus	3C84/3C111	18.6/2.6
	April – June 2013	19	Uranus	3C84/3C111	17.1/2.7
DEZ	February 2013	31	Uranus	3C84/3C111	20.7/3.9
EZ	August – September 2012	25	Uranus	3C84/3C111	18.0/3.1
	July – August 2013	50	Uranus	3C84/3C111	17.5/4.2

3. Continuum Results

We detected no compact continuum sources above the 5σ level of the 3 mm continuum map. One source was detected above 3σ that could be confirmed with other observations; L1451-mm (Pineda et al. 2011) is detected at 4σ with $5.2 \text{ mJy beam}^{-1}$. Figure 2 shows the 3 mm continuum image toward L1451-mm. The position, peak brightness, and lower-limit mass for our detection were calculated following the prescription described in Paper I and are listed in Table 3. The position and peak brightness agree with CARMA 3 mm measurements from Pineda et al. (2011), which had a $\sim 5''$ synthesized beam. Our image shows a possible secondary peak to the north of the brightest emission. However, this secondary peak is only within the $2\text{--}3\sigma$ contours and does not appear in the higher sensitivity observations of Pineda et al. (2011). Pineda et al. (2011) detected a low-velocity CO ($J = 2 \rightarrow 1$) outflow in this area; we do not detect any HCN or HCO⁺ outflow emission near this source.

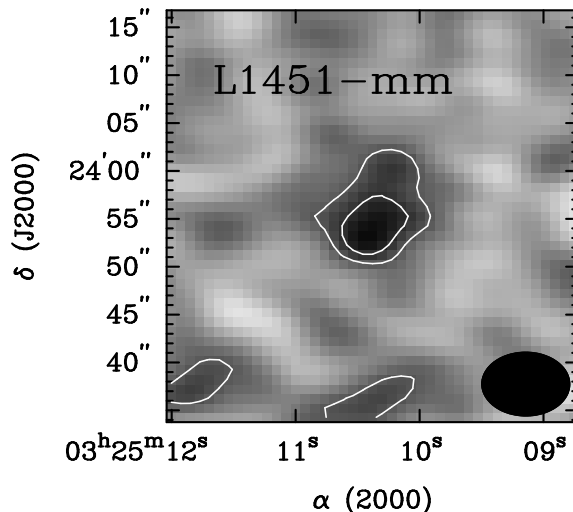


Fig. 2.— The single continuum detection in our field. The synthesized beam is $9.2'' \times 6.6''$, and the 1σ sensitivity is $1.3 \text{ mJy beam}^{-1}$. The contour levels are 2, 3 times 1σ ; no negative contours are present.

4. Morphology of Dense Molecular Gas

4.1. Integrated Intensity Emission

Figure 3 shows integrated intensity maps for HCO⁺, HCN, and N₂H⁺ ($J = 1 \rightarrow 0$) ($\sim 8''$ angular resolution), along with a *Herschel* 250 μm image ($18.1''$ angular resolution) for a visual comparison between the

Table 2. Correlator Setup Summary

Line	Rest Freq. (GHz)	No. Chan.	Chan. Width (MHz)	Vel. Coverage (km s^{-1})	Vel. Resolution (km s^{-1})	Chan. RMS (Jy beam^{-1})	Synth. Beam ^a
N ₂ H ⁺	93.173704 ^b	159	0.049	24.82	0.157	0.14	$8.6'' \times 6.8''$
Continuum	92.7947	47	10.4	1547	33.6	0.0013	$9.2'' \times 6.6''$
HCO ⁺	89.188518	159	0.049	25.92	0.164	0.12	$8.8'' \times 7.1''$
HCN	88.631847 ^c	159	0.049	26.10	0.165	0.12	$8.9'' \times 7.2''$

Note. — ^aThe synthesized beam is slightly different for each pointing center, and MIRIAD calculates a synthesized beam for the full mosaic based on all of the pointings. ^bThe rest frequency of the band was set to the weighted mean frequency of the center three hyperfine components. ^cThe rest frequency of the band was set to the frequency of the center hyperfine component. See <http://splatalogue.net> for frequencies of the HCN and N₂H⁺ hyperfine components.

dense gas and dust emission. The line maps were integrated over all channels with identifiable emission. The locations of the four Bolocam 1.1 mm sources (Enoch et al. 2006) and the one compact continuum core in L1451 are marked on each image of Figure 3. Four of the five sources are located near peaks of dense gas and dust emission. While the molecules and dust are tracing similar features around those sources, the exact morphological details vary. Below, we describe the qualitative emission features, and refer to the colored rectangles in Figure 3 for reference.

All tracers show a curved structure surrounding L1451-mm and the two nearby Bolocam sources (see red rectangle in Figure 3), with a peak of integrated emission at the location of L1451-mm. The southwestern edge of the curved structure has a stream of emission that extends further to the southwest (see dark blue rectangle in upper left panel of Figure 3), which can be seen in all the maps, though it extends furthest in the HCO^+ , HCN, and dust maps. The two other Bolocam sources to the far east of L1451-mm are surrounded by significant molecular gas structure (see green rectangle in lower left panel). The HCO^+ emission has the largest spatial extent in this region.

The integrated emission in the three lines is less similar across the western half of L1451 compared to the eastern half. There is a strong, condensed N_2H^+ source (see orange rectangle in lower right panel) that does not appear strongly in the HCN or HCO^+ maps, but that does correspond to a peak of emission in the dust map (see Section 8.3 for more details on this source). The strongest HCO^+ feature in the western half of the map has a weaker counterpart in the HCN map (see purple rectangle), which appears even weaker in N_2H^+ . Finally, there is HCO^+ emission to the northwest of the curved structure (see cyan rectangle) that closely mimics dust emission in that region; this emission is weakly detected in HCN, but not in N_2H^+ . Since the $J = 1 \rightarrow 0$ transition of HCO^+ traces densities about an order of magnitude lower than the other two molecules (Shirley 2015), the regions with strong HCO^+ and weak HCN and N_2H^+ are likely at lower density compared to regions where all the molecules have strong emission.

4.2. Channel Emission

Figure 4 shows channel maps of HCO^+ , HCN, and N_2H^+ highlighting the bulk of the emission, which occurs from ~ 4.8 to 3.5 km s^{-1} , with 2-channel spacing (e.g., we skip the 4.66 km s^{-1} channel between the 4.82 km s^{-1} and 4.50 km s^{-1} channels of HCO^+). In general, it is clear from the channel maps in Figure 4 that strong HCO^+ emission is more widespread compared to HCN emission, and particularly N_2H^+ emission (as was also evident in Figure 3). We label qualitative features in the HCO^+ channel maps, from A through I, in the order that they appear in velocity space (with eastern sources being labeled before western sources). We then place those same labels on the HCN and N_2H^+ maps to aid a qualitative comparison of dense gas features, given below.

Features A and C in the eastern half of the map are traced with all molecules, with varying strength. In Figure 4, Feature A appears strongly in HCO^+ at 4.82 km s^{-1} , faintly at 4.82 km s^{-1} in HCN, and not until

Table 3. Observed Properties of Continuum Detection

Source Name	Position (h:m:s, d:':")	Pk. Bright. (mJy beam ⁻¹)	Mass (M_\odot)
(1)	(2)	(3)	(4)
L1451-mm	03:25:10.38, +30:23:55.9	5.2 ± 1.3	0.10 ± 0.03

Note. — (3) Peak brightness, (4) Lower-limit mass using the peak brightness and assumptions outlined in Paper I.

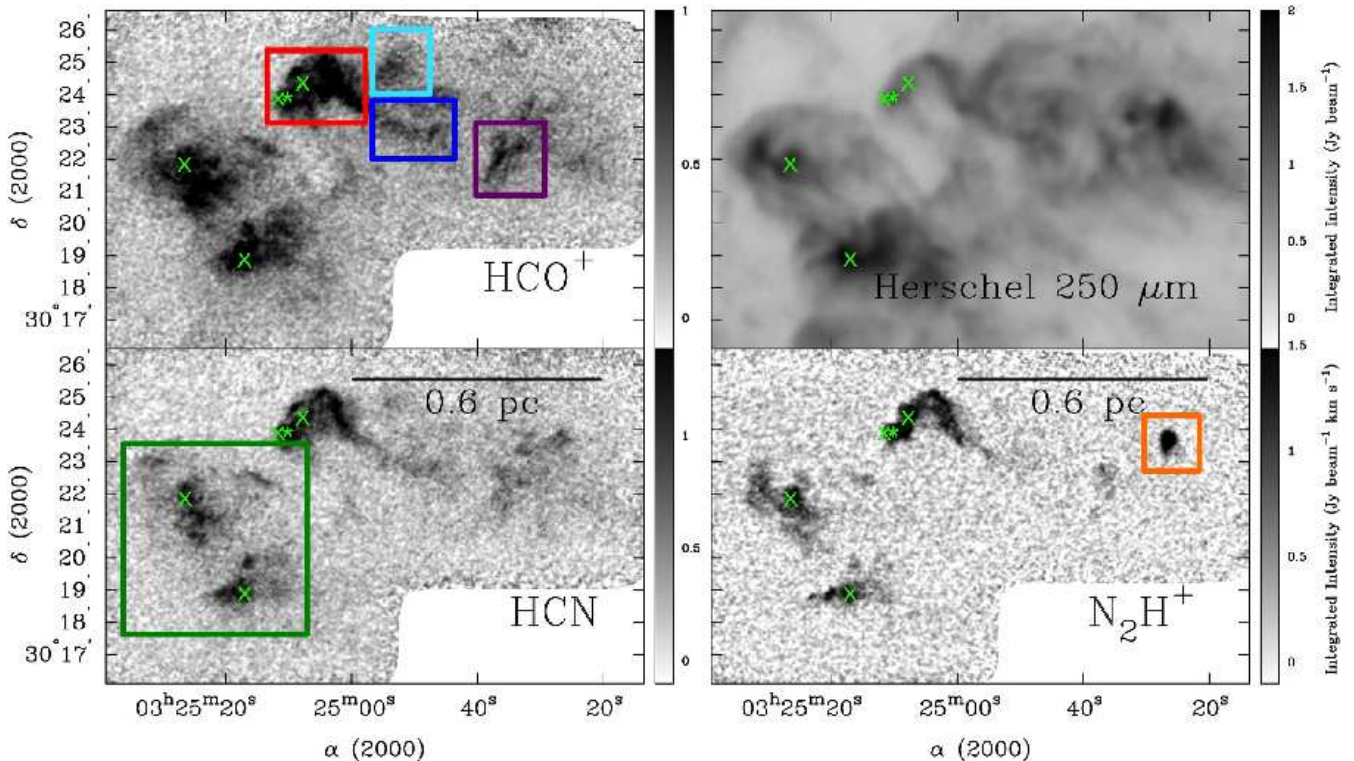


Fig. 3.— Integrated intensity maps of HCO^+ , HCN , and $\text{N}_2\text{H}^+(J = 1 \rightarrow 0)$ emission toward L1451, along with a *Herschel* 250 μm map of the region. HCO^+ emission was integrated from 5.316 to 3.018 km s^{-1} . HCN emission was integrated over all three hyperfine components from 9.945 to 7.962 km s^{-1} , 5.154 to 2.841 km s^{-1} , and -2.115 to -3.932 km s^{-1} . N_2H^+ emission was integrated over all seven hyperfine components over velocity ranges from 11.542 to 8.714 km s^{-1} , 5.729 to 2.744 km s^{-1} , and -3.383 to -4.639 km s^{-1} . The rms of the maps are 0.08, 0.13, and 0.16 $\text{Jy beam}^{-1} \text{km s}^{-1}$ for HCO^+ , HCN , and N_2H^+ , respectively. The four Bolocam 1.1 mm sources in this region are marked with “x” symbols, and the L1451-mm compact continuum core is marked with an asterisk. Colored rectangles show the locations of qualitative features discussed in Section 4.1.

4.47 km s^{-1} in N_2H^+ . Even when it finally appears as N_2H^+ emission, the emission is much more spatially concentrated than what we observe in HCO^+ and HCN . This spatial concentration is likely because the $\text{N}_2\text{H}^+(J = 1 \rightarrow 0)$ line traces higher-density, colder material compared to HCO^+ and $\text{HCN}(J = 1 \rightarrow 0)$ lines (Shirley 2015). A 1.1 mm Bolocam core is located within Feature A, and corresponds with a peak in the N_2H^+ emission. Feature A moves northeast to southwest from 4.82 km s^{-1} to lower-velocity channels as Feature C appears to its southwest. Features A and C are possibly part of the same larger-scale structure, which will be explored in the next section when we analyze the kinematics of this region. Like Feature A, Feature C is more spatially concentrated in N_2H^+ , and contains a 1.1 mm Bolocam source at an N_2H^+ peak of emission.

Feature B contains the L1451-mm compact continuum source. It appears strongly in all molecules, though it contains a prominent ridge of emission at 4.82 km s^{-1} in HCO^+ and HCN that does not appear in N_2H^+ near that velocity.

Features D, E, F, G, H, and I are all identified based on the HCO^+ emission. HCN emission appears weakly toward all features seen with HCO^+ , while N_2H^+ only shows faint emission in one channel for Features G and H at 3.84 km s^{-1} . The descriptions below are based on HCO^+ . Feature D appears to the west of Features A and C, and to the south of Feature B, seen at 4.50 km s^{-1} as an elliptical feature. Feature E appears as a prominent, round emission feature at 4.50 km s^{-1} , with more extended emission in channels surrounding the 4.50 km s^{-1} peak of emission. Feature F is emission that starts just to the northwest of Feature B at

4.17 km s⁻¹, peaks at 3.83 km s⁻¹, and then appears to get fainter while extending to the southwest at the unshown 3.67 km s⁻¹ channel, while then brightening to the southwest at 3.51 km s⁻¹. Feature G emission peaks at 3.83 km s⁻¹, and appears as a stream of emission to the east of Feature E. Feature H is a streamer to the southwest of Feature B and the south of Feature F, which first appears at 3.83 km s⁻¹. It persists at 3.51 km s⁻¹ and more faintly extends into two lower-velocity channels not shown in the figure. Feature I first appears at 3.51 km s⁻¹, brightens in two lower-velocity channels not shown in the figure, and is not detectable at velocities lower than that.

Feature J, referred to as L1451-west in the rest of the paper, is relatively round emission that only appears strongly in the N₂H⁺ data. It first appears at 4.79 km s⁻¹ in Figure 4, and is visible across a total of four velocity channels per hyperfine component—the structure can be seen repeating for another hyperfine component, starting in the 3.84 km s⁻¹ channel. We discuss details of the structure and kinematics of L1451-west in Section 8.3.

We detect no HCN or HCO⁺ outflow emission in any channel, which suggests that L1451 is a young region with little to no protostellar activity. Figure 5 show an example spectrum for each molecule from the location of L1451-mm within a single synthesized beam. The conversions from Jy beam⁻¹ to K for these data are 2.47 K/Jy beam⁻¹, 2.46 K/Jy beam⁻¹, and 2.42 K/Jy beam⁻¹ for HCO⁺, HCN, and N₂H⁺, respectively.

A small fraction of HCO⁺ and HCN spectra across L1451 show double peaks with a variety of line-shape characteristics—we estimate that ~3% of cloud locations show double-peak features. We cannot determine the absolute cause of the double peaks without H¹³CN and H¹³CO⁺ ($J = 1 \rightarrow 0$) observations at each cloud location, so analyzing these features is beyond the scope of this paper. However, the most likely scenario is self-absorption from a foreground screen of lower-density gas with a significant HCO⁺ and HCN ($J = 1 \rightarrow 0$) population. An infall scenario can be ruled out in many locations since infall predicts a stronger blue peak (Evans 1999) while we often observe stronger red peaks; a scenario with two-components along the same line-of-sight can likely be ruled out in many locations where the HCO⁺ and HCN spectra do not both show double-peaks.

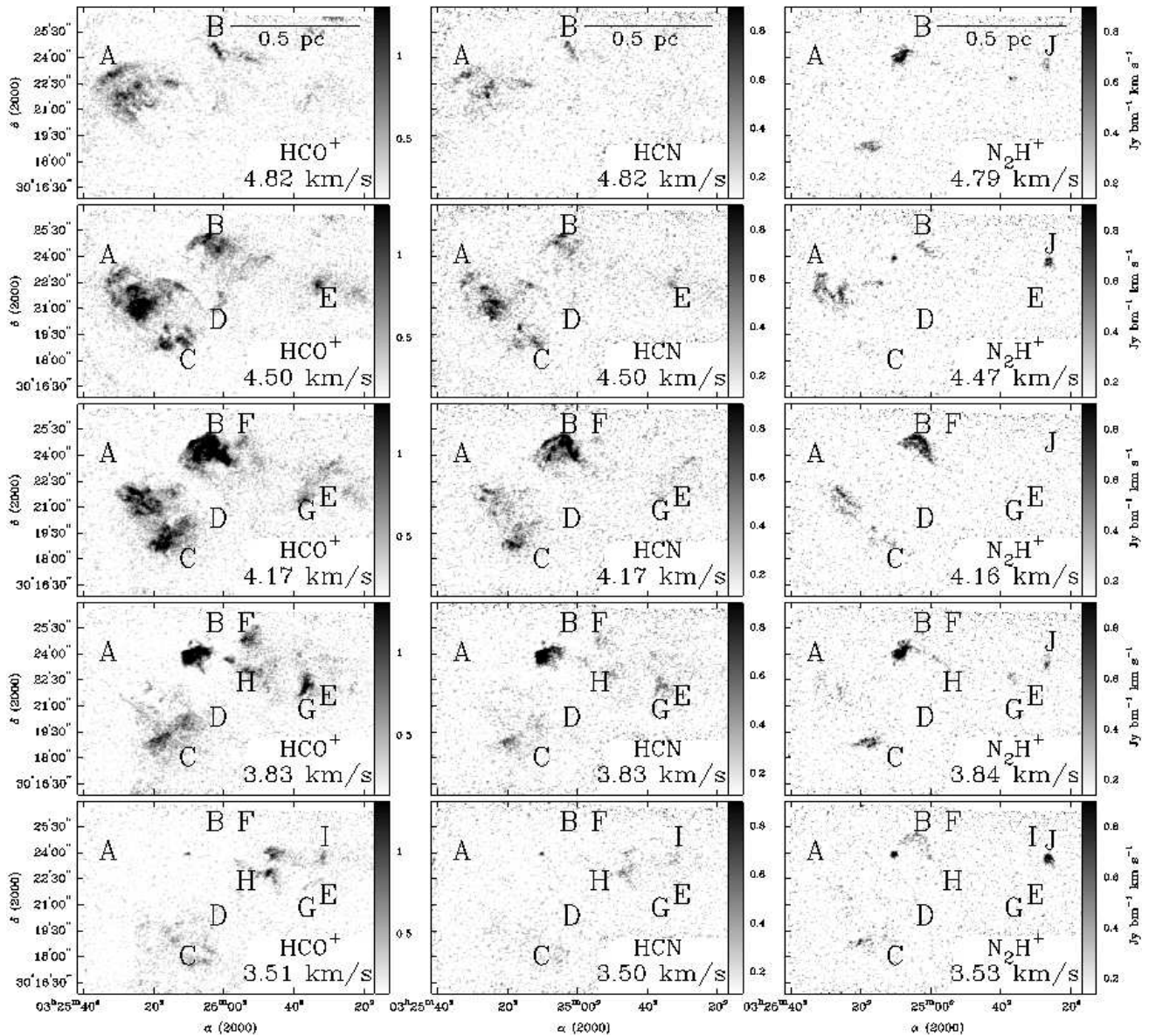


Fig. 4.— *Left*: Five HCO⁺ channels maps, with two-channel spacing. The rms in each channel is 0.12 Jy beam⁻¹, and the color intensity ranges from 0.12–1.3 Jy beam⁻¹. Features discussed in the text are identified with a letter in the first channel they appear. *Center*: Five HCN channels maps. The rms in each channel is 0.12 Jy beam⁻¹, and the color intensity ranges from 0.12–0.9 Jy beam⁻¹. Feature labels from the HCO⁺ maps are overplotted in the same locations for aid in comparing the emission across molecules. *Right*: Five N₂H⁺ channel maps. Note that several features appear twice across the channels due to the hyperfine structure of N₂H⁺. The rms in each channel map is 0.14 Jy beam⁻¹, and the color intensity ranges from 0.14–0.9 Jy beam⁻¹. Feature labels from the HCO⁺ maps are overplotted in the same locations for aid in comparing the emission across molecules. Feature J (also referred to as L1451-west) only appears in N₂H⁺, so it is only labeled in this figure.

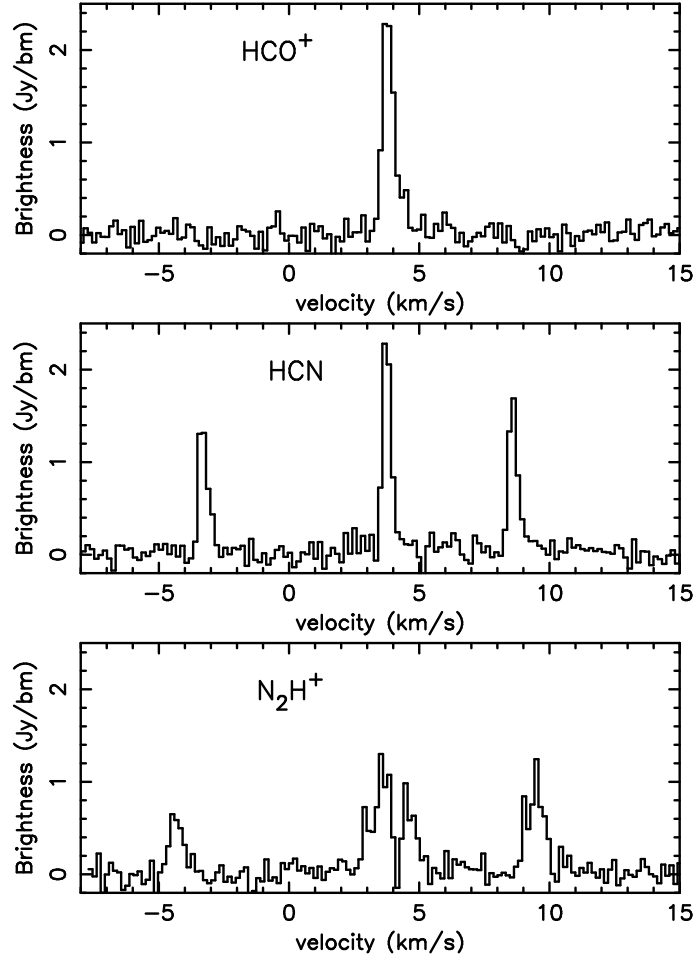


Fig. 5.— Example HCO⁺, HCN, and N₂H⁺ spectra from the location of L1451-mm reported in Table 3. Spectra are averaged over one synthesized beam, and the conversion factors from Jy beam⁻¹ to Kelvin are reported in the text.

5. Kinematics of Dense Molecular Gas

We fitted the molecular line emission presented in Section 4 with Gaussians using the method described in Paper I, and present the centroid velocity and line-of-sight velocity dispersion maps here. The seven resolvable hyperfine components of the N_2H^+ ($J = 1 \rightarrow 0$) line, and the three hyperfine components of the HCN ($J = 1 \rightarrow 0$) line, are simultaneously fit assuming the same velocity dispersion and excitation conditions for each component. HCO^+ ($J = 1 \rightarrow 0$) has no hyperfine splitting and is fit as a single Gaussian component.

We fit all the HCN and HCO^+ spectra with a single component across the entire field, even though about 3% of the spectra show evidence of double-peaks. To estimate the impact of fitting a double-peaked spectrum with a single component, we extrapolated several double-peaked spectra to a single peak, fit those single-peak spectra, and measured the full width at half of the extrapolated single-peak spectra. From those fits, we estimate that the velocity dispersions derived from the single-component fits to double-peaked spectra are overestimated by $\sim 10\%$. Considering that only about 3% of the spectra have this 10% overestimation, the double-peaks have a negligible impact on the results presented in this paper.

Although a low-velocity outflow from L1451-mm was previously detected in CO ($J = 2 \rightarrow 1$) by Pineda et al. (2011), we do not detect any outflow signatures in our HCN or HCO^+ ($J = 1 \rightarrow 0$) observations as we did in other CLASSy fields. Therefore, there are no line broadening effects from outflows that are impacting the line profile fits.

In Figure 6, we plot the fitted centroid velocity and velocity dispersion where: 1) the integrated intensity is greater than or equal to four times the rms of the integrated intensity map, and 2) the peak signal-to-noise of the spectrum is greater than five. We will use these kinematic maps in the following sections in order to interpret the hierarchical and turbulent nature of the region. Here we list some general features of interest pertaining to the maps:

1. HCO^+ has systematically larger line-of-sight velocity dispersion compared to HCN and N_2H^+ . The mean and standard deviation of the velocity dispersions across the maps are 0.29 ± 0.10 , 0.16 ± 0.07 , and 0.12 ± 0.04 km s^{-1} , for HCO^+ , HCN, and N_2H^+ , respectively. The observed mean velocity dispersions above should be compared to the isothermal sound speed of the mean gas particles in the cloud for determining the turbulence in the observed gas. Note that the thermal velocity dispersion of the mean gas particle in the cloud is different from the thermal velocity dispersion of an individual molecule. If we assume that the typical temperature in this region is 10 K based on ammonia observations of Bolocam cores (Rosolowsky et al. 2008a), then the isothermal sound speed between the mean gas particles would be ~ 0.2 km s^{-1} (assuming molecular weight per free particle of 2.33), while the isothermal sound speed between individual N_2H^+ particles would be ~ 0.05 km s^{-1} .

The N_2H^+ velocity dispersions are subsonic everywhere, the HCN velocity dispersions are subsonic in most cloud locations, and the HCO^+ velocity dispersions are transsonic to supersonic in most cloud locations. Note that even though N_2H^+ and HCN are subsonic in many areas of L1451, they are not exhibiting purely thermal velocity dispersions, which would be ~ 0.05 km s^{-1} for 10 K gas. The $J = 1 \rightarrow 0$ line of HCO^+ traces densities about an order of magnitude lower than that of HCN and N_2H^+ (see Shirley 2015). Therefore, we are likely observing the trend from supersonic to subsonic gas motions as gas goes from the larger, less-dense scales traced by HCO^+ to the smaller, more-dense scales traced by HCN and N_2H^+ . This is expected in a turbulent medium, where velocity dispersion scales proportionally with size (McKee & Ostriker 2007).

2. All three molecules are tracing gas with centroid velocities ranging from ~ 3.8 – 4.7 km s^{-1} . However, the HCO^+ gas extends to lower velocities, due to the gas in the Feature H streamer, which appears in the HCN maps, but is not strong enough to provide reliable kinematic measurements. HCO^+ also extends to

higher velocities, due to strong gas emission from the northeast part of Feature A, which is noticeable in the first channel of Figure 4.

3. The HCO^+ centroid velocities for Features A and C show a gradient from northeast to southwest. It is possible that this is a large, rotating piece of dense gas, which is fragmenting into denser components (e.g., the Bolocam 1 mm sources). It is also possible that the redshifted northeast section and the blueshifted southwest section represent independent components in the turbulent medium, or that they are merely projected along the same line of sight. Observations of optically thin tracers, and tracers of lower-density, larger-scale material are needed to help distinguish between these scenarios.
4. The gas in the eastern half of Feature B shows a velocity gradient along the length of the feature. It is most blueshifted at the southeastern end near the L1451-mm core, and becomes increasingly redshifted further away to the northwest. The gas immediately surrounding the L1451-mm compact continuum core has a centroid velocity pattern that is consistent with rotation (Pineda et al. 2011), and has velocity dispersions that increase toward the core center. L1451-west N_2H^+ velocity dispersions also peak at the core center, and we compare these two sources in detail in Section 8.3.
5. Our measurements of N_2H^+ centroid velocity and velocity dispersion towards L1451-mm agree well with the results in Pineda et al. (2011), in terms of absolute values measured and gradients across the source.

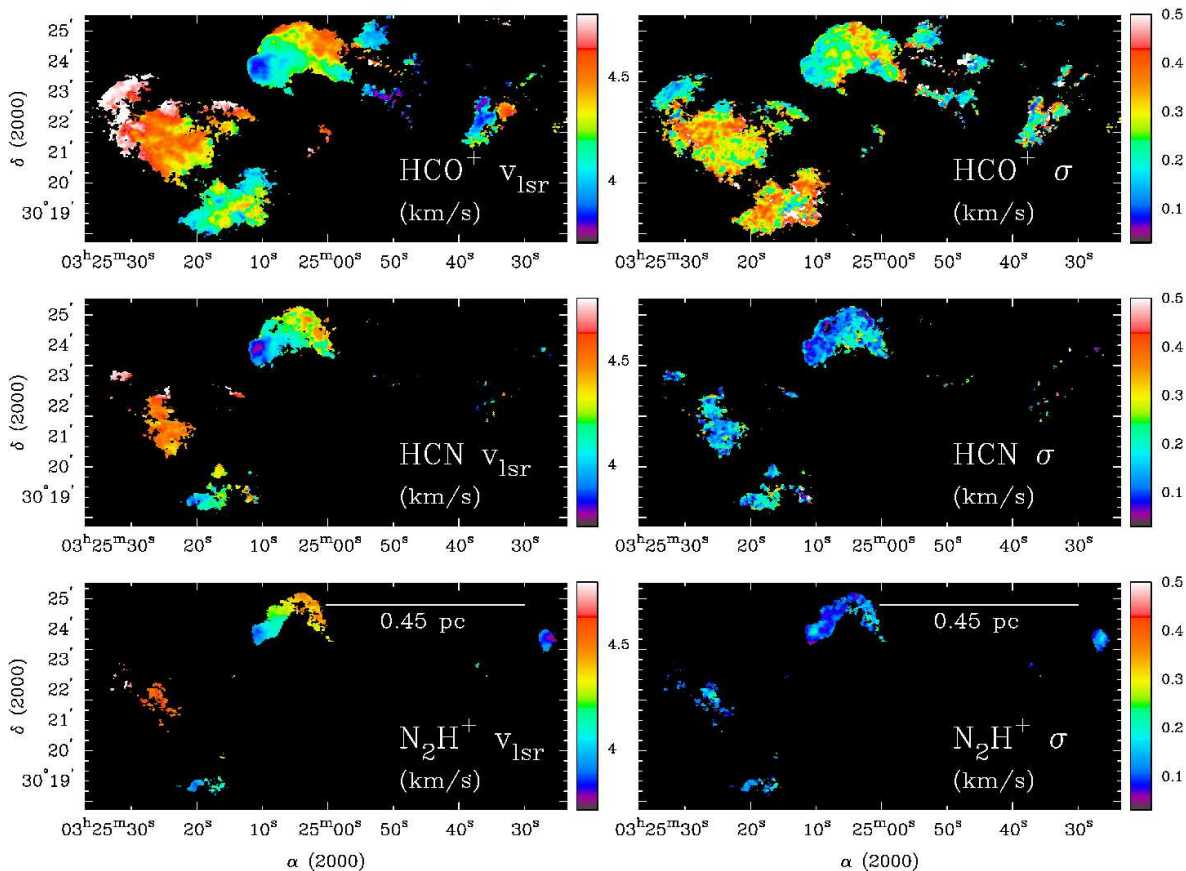


Fig. 6.— Kinematics of dense gas in L1451. *Left:* Centroid velocity (km s^{-1}) maps of HCO^+ , HCN , and N_2H^+ ($J = 1 \rightarrow 0$) emission, from top to bottom. *Right:* Line-of-sight velocity dispersion ($\text{FWHM}/2.355$ in km s^{-1}) maps of HCO^+ , HCN , and N_2H^+ ($J = 1 \rightarrow 0$) emission, from top to bottom. We masked these maps to visualize only statistically robust kinematic results (see Section 5 text). The color scales are the same across molecules.

6. Dendrogram Analysis of Molecular Emission

6.1. The Non-binary Dendrograms

We qualitatively described the dense gas morphology of L1451 in Section 4. Here we quantitatively identify dense gas structures from the three position-position-velocity (PPV) cubes and study the hierarchical nature of L1451 with the non-binary dendrogram algorithm described in Paper I.

A dendrogram algorithm identifies emission peaks in a dataset and keeps track of how those peaks merge together at lower emission levels. This method of identifying and tracking emission structures is advantageous compared to a watershed object-identification algorithm, such as CLUMPFIND (Williams et al. 1994), when the science goals include understanding how the morphology and kinematics of star-forming gas connects from large to small scales. A full discussion of the most widely used dendrogram algorithm applied to astronomical data can be found in Rosolowsky et al. (2008b); details of dendrograms and our non-binary version of the dendrogram algorithm are found in the appendices of Paper I, along with a comparison with the results from using a more standard clump-finding algorithm on our CLASSy data.

We ran our non-binary dendrogram algorithm on the HCO^+ emission, the emission from the strongest HCN hyperfine line, and the emission from the strongest N_2H^+ hyperfine line. For other CLASSy regions, we limited our analysis to N_2H^+ emission because the HCO^+ and HCN lines were complicated by protostellar outflows and severe self-absorption effects not seen in L1451. Also, for other CLASSy regions, we ran the algorithm on the N_2H^+ hyperfine component most isolated in velocity space because the strongest hyperfine component was often not spectrally resolved from adjacent components. The N_2H^+ hyperfine components in L1451 are resolved in all locations, letting us use the strongest component for our dendrogram analysis. A caveat is that some bluer emission from the higher-velocity, adjacent hyperfine component, and some redder emission from the lower-velocity, adjacent hyperfine component appear in the channels of the strongest component. Since there is no blending of hyperfine emission at the same location within the cloud, we masked the emission from the adjacent hyperfine components in the individual channels of the strongest hyperfine component in which they appeared. As an example, L1451-west (Feature J) appears in much bluer channels compared to Feature A, so L1451-west emission from the higher-velocity, adjacent hyperfine component also appears in the reddest channel of the strongest hyperfine component that shows Feature A. For this example, we masked out L1451-west emission from this red channel of the strongest component.

We ran the algorithm with similar parameters used for the Barnard 1 analysis described in Paper I, while following the prescription presented in Appendix A for comparing data cubes with different noise levels. The critical algorithm inputs and parameters were: (1) a masked input data cube with all pixels greater than or equal to 4σ intensity, along with pixels adjacent to the initial selection that are at least 2.5σ intensity, where σ is the rms level of the given data cube, (2) a set of local maxima greater than or equal to all their neighbors in $10''$ by $10''$ by three channel (0.94 km s^{-1}) spatial-velocity pixels to act as potential dendrogram leaves, (3) a requirement that a local maximum peak at least $2\text{-}\sigma_n$ above the intensity where it merges with another local maximum for a structure to be considered a leaf (referred to as the “`minheight`” parameter below and in Appendix A), where σ_n is the rms level of the noisiest data cube (N_2H^+ at $\sim 0.14 \text{ Jy beam}^{-1}$, in this case), and (4) a requirement of at least three synthesized beams of spatial-velocity pixels for a structure to be considered a leaf (referred to as the “`minpixel`” parameter below and in Appendix A). The `minheight` and `minpixel` parameters act to prevent noise features from being identified as dendrogram leaves. Branching steps are restricted to integer values of the $1\text{-}\sigma_n$ sensitivity of the data (referred to as the “`stepsize`” parameter below and in Appendix A) for our non-binary dendrograms when comparing datasets with different noise-levels. Appendix A shows that using uniform `minheight` and `stepsize` allows a comparison of dendrogram properties that minimizes the impact of noise-level differences between data cubes.

Figures 7, 8, and 9 show HCO^+ , HCN, and N_2H^+ non-binary dendrograms for L1451, respectively. The vertical axis of the dendrograms represent the intensity range of the pixels belonging to a leaf or branch. The

horizontal axis is arranged with the major features identified in Figure 4 progressing from east-to-west; we label certain branches that are associated with major features, and we provide the numeric label for structures referred to in the upcoming discussion. The isolated leaves are presented in numerical order. The horizontal dotted line in each dendrogram represents an intensity cut at $2.5\text{-}\sigma_n$ that aids in cross-comparison of dendrogram statistics (see Appendix A) and is discussed in Section 6.3.

The HCO^+ dendrogram contains the largest number of structures, with 86 leaves and 27 branches. The HCN dendrogram contains 33 leaves and 13 branches, while the N_2H^+ dendrogram only contains 16 leaves and 6 branches. Leaves that peak at least $6\text{-}\sigma_n$ in intensity above the branch they merge directly into are colored green and referred to as high-contrast leaves². The strongest leaf for every molecule is at or near the location of L1451-mm in Feature B: Leaf 66 is the strongest structure in the HCO^+ dendrogram, with a peak intensity of $2.78 \text{ Jy beam}^{-1}$, leaf 30 is the strongest structure in the HCN dendrogram, with a peak intensity of $2.58 \text{ Jy beam}^{-1}$, and leaf 10 is the strongest structure in the N_2H^+ dendrogram, with a peak intensity of $1.62 \text{ Jy beam}^{-1}$.

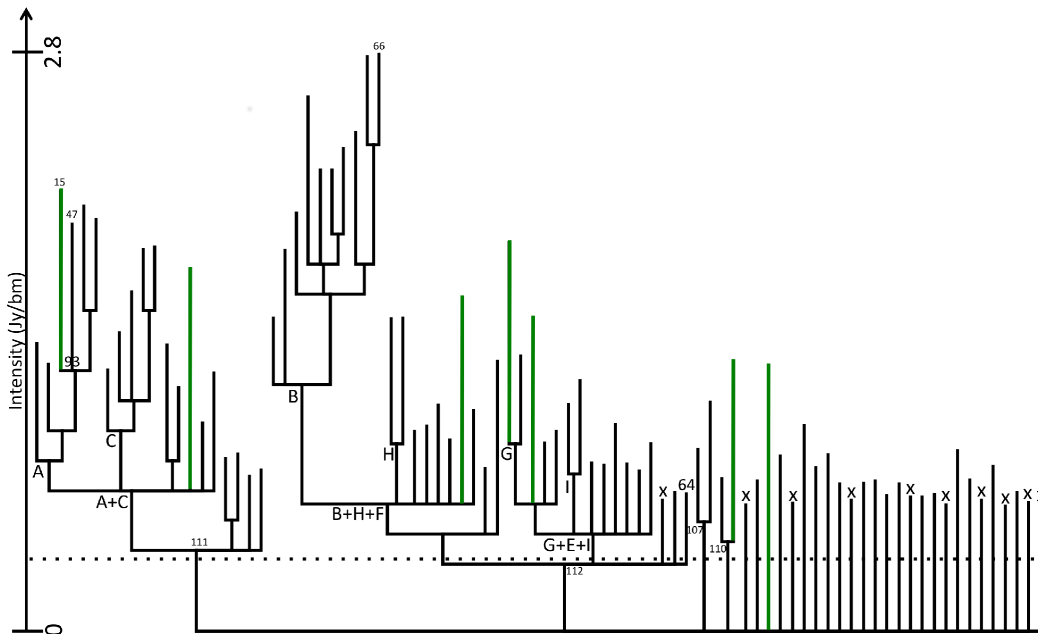


Fig. 7.— The HCO^+ non-binary dendrogram for L1451. The vertical axis represents the Jy beam^{-1} intensity for a given location within the gas hierarchy. The horizontal axis is ordered so that features identified in Section 4 are generally ordered from east to west. Leaves and branches discussed in the text are labeled with their numerical identifier, and branches associated with major features from Section 4 are marked with the feature letter. The leaves colored green peak at least $6\text{-}\sigma_n$ above their first merge level. The horizontal dotted line represents the $2.5\text{-}\sigma_n$ intensity cut above which we calculate tree statistics *when comparing dendrograms made from data with different noise levels*. The leaves labeled “x” are discarded from the calculation of tree statistics when comparing the dendrograms of different molecules observed with different noise levels, but they are used when studying the structure of an individual dendrogram.

²We will use the definition of high-contrast leaves, first introduced in Paper I, as a way of comparing the properties of strong leaves across CLASSy clouds in future papers.

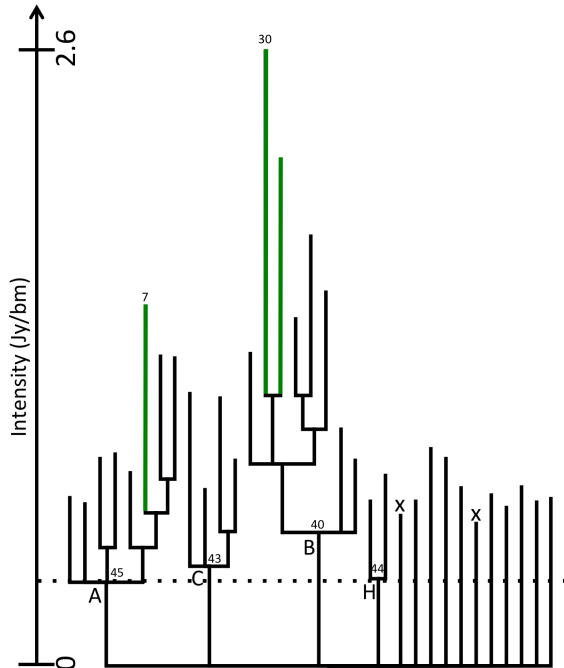


Fig. 8.— Same as Figure 7, but for the HCN non-binary dendrogram.

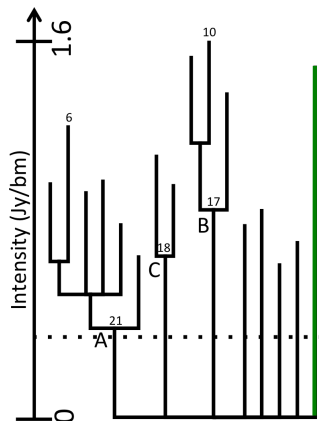


Fig. 9.— Same as Figure 7, but for the N_2H^+ non-binary dendrogram.

6.2. Dendrogram Spatial and Kinematics Properties

The leaves and branches of each dendrogram represent molecular structures. We fit for the spatial properties of each structure, as we did in Paper I, using the `regionprops` program in MATLAB. This program fits an ellipse to the integrated intensity footprint of each dendrogram structure to determine its RA centroid, DEC centroid, major axis, minor axis, and position angle. Columns 2–6 in Tables 4–6 list the spatial properties of each structure. To quantify the shape of each structure, we use the axis ratio and filling factor of the fit (Columns 7 and 8 of Tables 4–6). We lastly define the structure size (Column 9 of Tables 4–6) as the geometric mean of the major and minor axes, assuming a distance of 235 pc when converting to parsec units.

Histograms of the size, filling factor, and axis ratio for all leaves and branches are plotted in the top rows of Figures 10–12. All HCO^+ and HCN leaves are smaller than 0.12 pc, while all N_2H^+ leaves are smaller than 0.06 pc. HCO^+ branches are the largest of all molecules, peaking at 0.46 pc, while HCN branches peak

at 0.24 pc, and N_2H^+ branches peak at 0.17 pc. This is expected since HCO^+ shows the most widespread emission in the channel and integrated emission maps. The filling factor for all molecular structures is between 0.45 and 0.95. The structures with filling factor closest to unity are leaves, indicating that leaves are more likely to be elliptically shaped objects while branches are more likely to be irregularly shaped objects. The axis ratio for all structures is between 0.19 and 0.95, showing that there is a distribution from elongated to round structures, without strong differences between leaves and branches. There are no obvious differences between the high-contrast leaves and the rest of the leaves.

We use the integrated intensity footprints of the dendrogram structures in combination with the centroid velocity and velocity dispersion maps to determine kinematic properties of leaves and branches. The four properties present in Tables 4–6 are: mean and rms centroid velocity ($\langle V_{\text{lsr}} \rangle$ and ΔV_{lsr} , respectively), and mean and rms velocity dispersion ($\langle \sigma \rangle$ and $\Delta \sigma$, respectively). We illustrated how to derive these properties for leaves and branches in Section 6 of Paper I.

Histograms of $\langle V_{\text{lsr}} \rangle$, ΔV_{lsr} , and $\langle \sigma \rangle$ are plotted in the bottom rows of Figures 10–12. HCO^+ traces larger variation in $\langle V_{\text{lsr}} \rangle$ compared to HCN and N_2H^+ . We attribute this to HCO^+ being sensitive to more widespread emission away from the densest regions of L1451, and therefore tracing more widespread centroid velocities relative to the systemic velocity of the most spatially compact gas. For all molecules, ΔV_{lsr} of the leaves generally extends from low to moderate velocities, while it is distributed from moderate to high velocities for the branches. This indicates a trend where ΔV_{lsr} is generally lower for smaller structures than larger structures. This trend was also seen for Barnard 1 gas structures, and we discussed explanations in Paper I; the primary reason was the scale-dependent nature of turbulence, which causes gas parcels separated by smaller distances to have smaller rms velocity differences between them (McKee & Ostriker 2007).

The distribution of $\langle \sigma \rangle$ is similar for leaves and branches, with neither distribution showing a preference to peak at high or low velocities. This trend was also seen in Paper I for Barnard 1, indicating that $\langle \sigma \rangle$ does not strongly depend on the projected size of a structure. The peak $\langle \sigma \rangle$ for HCO^+ is higher compared to HCN and N_2H^+ : 0.42 km s^{-1} , 0.18 , and 0.13 km s^{-1} , respectively. Since HCO^+ traces effective excitation densities of an order of magnitude lower than HCN and N_2H^+ (Shirley 2015), we are likely observing emission from lower-density gas that is more extended along the line-of-sight. This could increase the line-of-sight velocity dispersions, which are expected to scale with cloud depth in a turbulent medium (McKee & Ostriker 2007). There are no obvious differences in these kinematic properties between the high-contrast leaves and the rest of the leaves.

6.3. Tree Statistics

The dendrograms in Figures 7–9 show an apparently wide variety of hierarchical complexity between molecular tracers and between sub-regions of L1451. In this section, we quantify the hierarchical nature of the gas with tree statistics that were introduced and explained in Paper I so that the complexity between molecules and sub-regions can be quantitatively compared. Specifically, we calculate the maximum branching level, mean path length, and mean branching ratio of the entire L1451 region for each molecule in a uniform way that accounts for differences in the noise-level of each data cube (see Appendix A). We then calculate those same statistics for individual features within each dendrogram.

To compare the tree statistics of the dendrograms from the different molecular tracers we follow Appendix A and only consider leaves and branches above a $2.5\text{-}\sigma_n$ intensity cut, where σ_n is the rms of the noisiest molecular data cube. The N_2H^+ PPV cube has the highest noise level, at $\sim 0.14 \text{ Jy beam}^{-1}$, so the cut for each dendrogram is at $\sim 0.35 \text{ Jy beam}^{-1}$, and is represented as the horizontal dotted line in Figures 7–9. Only leaves that peak at least $2\text{-}\sigma_n$ above the cut are still considered in the statistics—all other leaves are marked with an “x” in the dendrograms. A branch below the cut is discounted, but if the leaf directly above it is more than $2\text{-}\sigma_n$ above the

cut, then the leaf is counted as a leaf with a branching level of zero (e.g., leaf 64 in Figure 7). This comparison of tree statistics ensures that we can compare the hierarchical structure of emission from the different molecules independent of noise-level differences introduced from the observing setup. These considerations are not needed when comparing tree statistics from sub-regions of a single dendrogram.

The path length statistic, defined only for leaves, is the number of branching levels it takes to go from a leaf to the tree base. The branching ratio statistic, defined only for branches, is the number of structures a branch splits into immediately above it in the dendrogram. We will be linking these tree statistics to cloud fragmentation in the discussion to follow. A more evolved region with a lot of hierarchical structure will have a higher maximum branching level and larger mean path length than a young region that is starting to form overdensities and fragment. The branching ratio of a very hierarchical region will be smaller than a region fragmenting into many substructures in a single step. This is likely an overly simplistic view, since the molecular emission, and in turn, the dendrograms and tree statistics, can also be affected by projection effects and line opacity. We briefly discussed these effects in Paper I; since they are extremely difficult to accurately model over such a large area, we use the simple view that hierarchy comes from fragmentation³.

The tree statistics of each dendrogram from the different molecular tracers are reported in the first section of Table 7. The mean branching ratios are 3.8, 3.3, and 3.1 for the HCO^+ , HCN, and N_2H^+ emission, respectively. We interpret this to mean that each molecule is tracing physical structures that are fragmenting in a hierarchically similar way (e.g., a structure is most likely to fragment into about three to four sub-structures). The mean path length of HCO^+ is 1.0 level longer than that of HCN and N_2H^+ , and the maximum branching level of HCO^+ is two more than that of HCN and three more than that of N_2H^+ . This trend in fragmentation levels is likely due to the ability of each tracer to detect material at different spatial scales and physical densities. As the effective excitation density of the tracer goes down from N_2H^+ to HCN to HCO^+ , our observations are more sensitive to more widespread emission, which means we are sensitive to more levels of fragmentation extending from the higher-density leaves (detectable with all tracers) to the lowest detectable branches (most detectable with HCO^+). Therefore, even though the dendrograms in Figures 7–9 look very different, a comparison of their tree statistics using a uniform noise-level cut, along with an understanding of what each molecule is tracing, produces a consistent picture of the hierarchical structure of dense gas in L1451 from ~ 0.5 pc to sub-0.1 pc scales.

The tree statistics of sub-regions from individual molecular tracers are reported in the second section of Table 7. We compare the sub-region statistics of Features A, B, C, and all other features with hierarchical complexity (e.g., Feature H in the HCO^+ and HCN dendrograms). The sections of the dendrograms corresponding to individual features are marked in Figures 7–9 with letter identifiers, and we only consider structures above those identifiers in this comparison. For example, in the HCO^+ dendrogram, Features A and C merge together at the branch labeled “A+C,” but we consider the statistics of the individual features only above labels “A” and “C”. Features A, B, and C are the only features with any hierarchical complexity in the N_2H^+ dendrogram, and are the ones with the most branching steps in the HCN and HCO^+ dendrograms. They are also the most likely sites for current and future star formation, since they account for emission surrounding the only continuum source detections in the field: Feature B surrounds L1451-mm, and Features A and C surround Bolocam 1 mm sources.

There is a trend of decreasing maximum branching level and mean path length from Feature B to A to C and then to the other remaining features. Features A and B are more similar to each other than either is to

³Although a few regions within L1451 show double-peaked HCO^+ spectra, which we attribute primarily to self-absorption and not true multiple components, the dendrogram algorithm rarely splits structures containing such spectral features in two. We searched the dendrogram structure cube and data cube by eye, and determined that only leaves 15 and 47 are likely split due to these double-peaked spectra. Accounting for this would reduce the branching ratio of branch 93 from three to two, have no effect on the maximum branching level, and have negligible impact on the average tree statistics. Therefore, we do not consider the HCO^+ dendrogram to be contaminated by double-peaked spectra.

the remaining other features, indicating that the gas in both features has fragmented a similar amount relative to the rest of the complex structure in the L1451 field. The mean path length and maximum branching level of Feature C bridge the gap between the maximum fragmentation amount seen in Feature A and B and the minimum fragmentation amount seen in the remaining other features.

We interpret the similarity in hierarchical branching levels between Features A and B to mean that these sub-regions have progressed to a similar stage along the evolutionary track of cloud fragmentation. We know a young star or first core (L1451-mm) is forming within Feature B at or near the location of the maximum gas emission intensity (leaf 66, 30, and 10 for HCO^+ , HCN , and N_2H^+ , respectively). For Feature A, PerBolo 6 is at or near the location of maximum gas emission intensity in Feature A (leaf 15, 7, and 6 for HCO^+ , HCN , and N_2H^+ , respectively). We argue that with Feature A and B showing very similar tree statistics, with Feature B having a confirmed compact continuum detection at its hierarchical peak, and with Feature A having a single-dish continuum detection at its hierarchical peak, that a star is likely to form within Feature A. This argument can be extended to Feature C being the next most likely place for current or future star formation, followed by the even less fragmented features. Follow-up observations of the single-dish cores and other column density enhancements in these features will be useful for testing this expectation. The mean branching ratios between all features are similar for all molecules, indicating that all structures are fragmenting into a similar number of sub-structures at each branching step, regardless how far a feature is along its evolution toward forming stars.

Table 4. HCO⁺ Dendrogram Leaf and Branch Properties

No.	RA	DEC	Maj. Axis	Min. Axis	PA	Axis	Filling	Size	$\langle V_{\text{lsr}} \rangle$	ΔV_{lsr}	$\langle \sigma \rangle$	$\Delta \sigma$	Pk. Int.	Contrast	Level
(1)	(h:m:s)	(°:′:″)	(″)	(″)	(°)	Ratio	Factor	(pc)	(km s ⁻¹)	(km s ⁻¹)	(km s ⁻¹)	(km s ⁻¹)	(Jy beam ⁻¹)	(15)	(16)
Leaves															
13	03:25:31.6	+30:21:34.6	18.1	14.7	105.5	0.81	0.86	0.019	4.72(2)	0.04(2)	0.21(2)	0.04(2)	1.29	2.2	4
14	03:25:01.2	+30:21:13.7	140.5	65.4	139.4	0.47	0.62	0.109	4.63(2)	0.09(2)	0.21(2)	0.07(1)	0.99	4.8	0
15	03:25:26.1	+30:21:54.4	56.7	42.0	134.6	0.74	0.71	0.056	4.55(1)	0.05(1)	0.30(1)	0.05(1)	2.12	6.0	5
16	03:25:31.1	+30:22:56.5	117.4	53.9	121.4	0.46	0.75	0.091	4.76(1)	0.06(0)	0.17(0)	0.04(0)	1.74	7.4	2
17	03:24:55.8	+30:24:31.8	22.8	13.1	81.8	0.57	0.86	0.020	4.46(3)	0.06(2)	0.41(1)	0.03(1)	1.09	3.3	3
Branches															
86	03:25:09.8	+30:23:52.9	47.6	42.9	118.3	0.90	0.73	0.051	3.89(1)	0.06(1)	0.19(1)	0.03(0)	2.35	...	6
87	03:25:03.4	+30:24:39.6	50.3	38.0	54.4	0.75	0.65	0.050	4.32(2)	0.07(1)	0.29(1)	0.04(1)	1.91	...	6
88	03:25:02.7	+30:24:17.9	110.8	59.8	49.9	0.54	0.68	0.093	4.20(2)	0.10(1)	0.26(1)	0.05(1)	1.77	...	5
89	03:25:09.3	+30:24:03.8	89.4	53.3	161.4	0.60	0.65	0.079	4.03(2)	0.11(2)	0.21(1)	0.03(1)	1.77	...	5
90	03:25:05.0	+30:24:13.9	186.3	102.2	93.1	0.55	0.75	0.157	4.18(1)	0.16(1)	0.24(0)	0.04(0)	1.62	...	4

Note. — Table 4 is published in its entirety in a machine readable format in the *Astrophysical Journal* online edition of this paper. A portion is shown here for guidance regarding its form and content.

Note. — (2)–(6) The position, major axis, minor axis, and position angle were determined from `regionprops` in MATLAB. We do not report formal uncertainties of these values since the spatial properties of irregularly shaped objects is dependent on the chosen method.

(7) Axis ratio, defined as the ratio of the minor axis to the major axis.

(8) Filling factor, defined as the area of the leaf or branch inscribed within the fitted ellipse, divided by the area of the fitted ellipse.

(9) Size, defined as the geometric mean of the major and minor axes, for an assumed distance of 235 pc.

(10) The weighted mean V_{lsr} of all fitted values within a leaf or branch. Weights are determined from the statistical uncertainties reported by the IDL MPFIT program. The error in the mean is reported in parentheses as the uncertainty in the last digit. It was computed as the standard error of the mean, $\Delta V_{\text{lsr}}/\sqrt{N}$, where ΔV_{lsr} is the value in column 11 and N is the number of beams’ worth of pixels within a given object. We report kinematic properties only for objects that have at least three synthesized beams’ worth of kinematic pixels.

(11) The weighted standard deviation of all fitted V_{lsr} values within a leaf or branch. The error was computed as the standard error of the standard deviation, $\Delta V_{\text{lsr}}/\sqrt{2(N-1)}$, assuming the sample of beams was drawn from a larger sample with a Gaussian velocity distribution.

(12) The weighted mean velocity dispersion of all fitted values within a leaf or branch. The error was computed as the standard error of the mean, $\Delta \sigma/\sqrt{N}$.

(13) The weighted standard deviation of all fitted velocity dispersion values within a leaf or branch. The error was computed as the standard error of the standard deviation, $\Delta \sigma/\sqrt{2(N-1)}$.

(14) For a leaf, this is the peak intensity measured in a single channel in the dendrogram analysis. For a branch, this is the intensity level where the leaves above it merge together.

(15) “Contrast” is defined as the difference between the peak intensity of a leaf and the height of its closest branch in the dendrogram, divided by $1-\sigma_n$.

(16) The branching level in the dendrogram. For example, the base of the tree is level 0, so an isolated leaf that grows directly from the base is considered to be at level 0. A leaf that grows from a branch one level above the base will be at level 1, etc.

Table 5. HCN Dendrogram Leaf and Branch Properties

No.	RA	DEC	Maj. Axis	Min. Axis	PA	Axis	Filling	Size	$\langle V_{\text{lsr}} \rangle$	ΔV_{lsr}	$\langle \sigma \rangle$	$\Delta \sigma$	Pk. Int.	Contrast	Level
(1)	(h:m:s)	($^{\circ}$: $'$: $''$)	($''$)	($''$)	($^{\circ}$)	Ratio	Factor	(pc)	(km s^{-1})	(km s^{-1})	(km s^{-1})	(km s^{-1})	(Jy beam^{-1})	(15)	(16)
Leaves															
5	03:25:24.1	+30:21:03.2	71.4	41.7	162.3	0.58	0.59	0.062	4.49(1)	0.05(1)	0.13(1)	0.03(0)	1.29	3.5	4
6	03:25:25.4	+30:21:45.4	27.1	19.7	82.7	0.73	0.86	0.026	4.56(2)	0.06(1)	0.15(1)	0.04(1)	1.30	3.6	4
7	03:25:26.3	+30:22:10.6	37.0	20.7	112.3	0.56	0.80	0.031	4.60(2)	0.06(1)	0.13(1)	0.06(1)	1.51	6.0	3
8	03:25:31.6	+30:22:59.0	53.1	29.1	101.8	0.55	0.72	0.045	4.73(1)	0.04(1)	0.11(1)	0.04(1)	0.89	2.7	2
9	03:25:28.4	+30:23:09.9	46.9	26.4	18.9	0.56	0.57	0.040	0.68	2.3	1
Branches															
33	03:25:03.0	+30:24:41.8	58.4	46.1	37.9	0.79	0.67	0.059	4.30(2)	0.08(2)	0.15(1)	0.05(1)	1.14	...	3
34	03:25:09.5	+30:24:03.4	92.4	47.2	158.3	0.51	0.78	0.075	4.00(2)	0.10(1)	0.11(0)	0.03(0)	1.14	...	2
35	03:25:02.7	+30:24:32.7	112.1	44.4	37.4	0.40	0.68	0.080	4.28(2)	0.11(2)	0.15(1)	0.05(1)	0.99	...	2
36	03:25:05.6	+30:24:16.7	180.1	100.9	103.4	0.56	0.75	0.154	4.17(1)	0.14(1)	0.12(1)	0.06(0)	0.85	...	1
37	03:25:24.6	+30:21:11.0	98.8	64.4	21.4	0.65	0.65	0.091	4.50(1)	0.06(1)	0.14(1)	0.04(0)	0.78	...	3

Note. — Table 5 is published in its entirety in a machine readable format in the *Astrophysical Journal* online edition of this paper. A portion is shown here for guidance regarding its form and content.

Note. — Columns the same at Table 4.

Table 6. N_2H^+ Dendrogram Leaf and Branch Properties

No.	RA	DEC	Maj. Axis	Min. Axis	PA	Axis	Filling	Size	$\langle V_{\text{lsr}} \rangle$	ΔV_{lsr}	$\langle \sigma \rangle$	$\Delta \sigma$	Pk. Int.	Contrast	Level
(1)	(h:m:s)	($^{\circ}$: $'$: $''$)	($''$)	($''$)	($^{\circ}$)	Ratio	Factor	(pc)	(km s^{-1})	(km s^{-1})	(km s^{-1})	(km s^{-1})	(Jy beam^{-1})	(15)	(16)
Leaves															
6	03:25:26.0	+30:21:44.0	51.1	36.0	30.7	0.70	0.66	0.049	4.57(1)	0.04(1)	0.13(1)	0.03(1)	1.25	4.0	3
7	03:25:03.9	+30:25:00.3	36.8	19.6	89.7	0.53	0.68	0.031	4.45(1)	0.03(1)	0.09(1)	0.02(0)	1.40	3.5	1
8	03:25:16.1	+30:19:47.4	35.7	28.9	54.8	0.81	0.68	0.037	0.89	3.7	0
9	03:24:55.8	+30:23:23.3	19.3	11.6	61.8	0.60	0.77	0.017	0.66	2.1	0
10	03:25:07.3	+30:24:32.1	38.5	21.1	96.6	0.55	0.71	0.032	4.24(1)	0.03(1)	0.08(0)	0.01(0)	1.62	3.0	2
Branches															
16	03:25:08.5	+30:24:11.8	101.3	38.3	136.7	0.38	0.71	0.071	4.11(2)	0.12(1)	0.10(0)	0.02(0)	1.18	...	1
17	03:25:04.8	+30:24:18.4	196.1	108.9	95.0	0.56	0.62	0.166	4.26(2)	0.17(1)	0.11(0)	0.03(0)	0.90	...	0
18	03:25:17.7	+30:18:54.8	141.7	42.6	101.8	0.30	0.65	0.088	4.08(2)	0.07(2)	0.13(1)	0.04(1)	0.69	...	0
19	03:25:25.6	+30:21:34.2	96.5	65.4	41.1	0.68	0.62	0.091	4.58(1)	0.04(1)	0.10(1)	0.02(0)	0.67	...	2
20	03:25:27.2	+30:21:45.9	200.6	100.1	53.0	0.50	0.56	0.161	0.53	...	1

Note. — Table 6 is published in its entirety in a machine readable format in the *Astrophysical Journal* online edition of this paper. A portion is shown here for guidance regarding its form and content.

Note. — Columns the same as Table 4.

Table 7. Tree Statistics

Line (Sub-region)	Total No. ^a	Max Level ^b	Mean PL ^c	Mean BR ^d
Comparison Across Tracers^e				
HCO ⁺	113	6	2.3	3.8
HCN	46	4	1.3	3.3
N ₂ H ⁺	22	3	1.3	3.1
Comparison of Sub-Regions^f				
HCO ⁺ (A)	10	6	4.8	2.3
HCO ⁺ (B)	16	7	5.9	2.5
HCO ⁺ (C)	8	5	4.2	2.3
HCO ⁺ (others)	9	4	3.7	2.0
HCN (A)	13	4	2.4	2.4
HCN (B)	13	4	2.6	2.4
HCN (C)	6	2	1.5	2.5
HCN (others)	3	1	1.0	2.0
N ₂ H ⁺ (A)	9	3	2.2	2.7
N ₂ H ⁺ (B)	5	2	1.7	2.0
N ₂ H ⁺ (C)	3	1	1.0	2.0
N ₂ H ⁺ (others)	NA	NA	NA	NA

Note. — ^a Total number of leaves and branches. ^b Maximum branching level tree statistic. ^c Mean path length tree statistic. ^d Mean branching ratio tree statistic. ^e Using method for comparing dendrograms of data with different noise levels, where only structures above the horizontal dotted line in Figures 7–9 without an “x” symbol are used to calculate tree statistics. ^f Using original dendrogram of the individual molecular tracer, where all structures are used to calculate tree statistics.

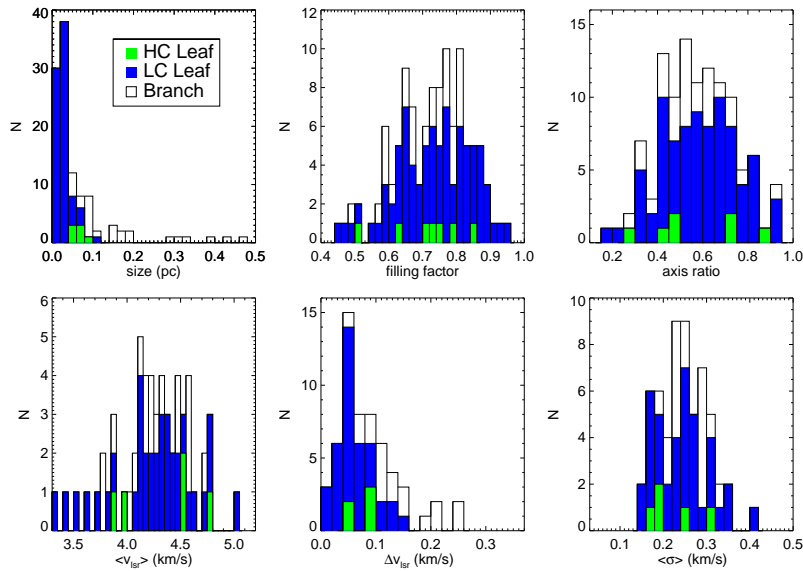


Fig. 10.— Histograms of HCO^+ dendrogram leaf and branch properties. High-contrast (HC) leaves, above $6\text{-}\sigma_n$ contrast, are represented by green; low-contrast (LC) leaves, below $6\text{-}\sigma_n$ contrast, are represented by blue; branches are represented by white. See the text in Section 6.2 for a discussion of trends seen in these histograms.

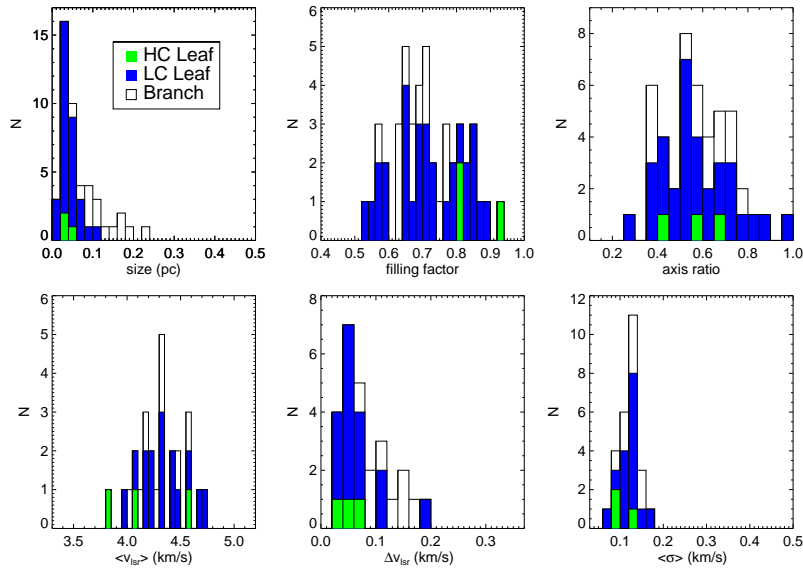


Fig. 11.— Same as Figure 10, but for HCN.

7. Dust in L1451

The CLASSy observations provide excellent measurements of gas structure and kinematics, but are less reliable for column density or mass information due to large uncertainties in relative abundance and opacity of the molecular emission. For this, we turned to *Herschel* observations.

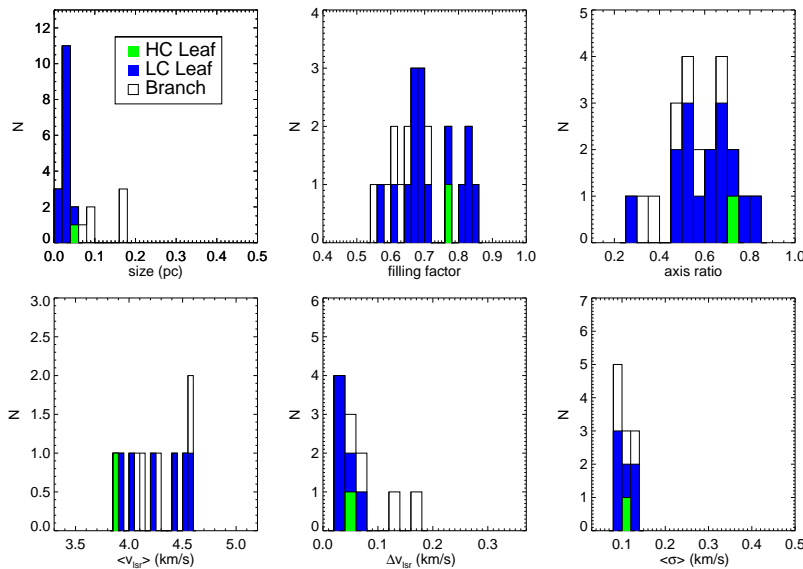


Fig. 12.— Same as Figure 10, but for N_2H^+ .

7.1. L1451 Column Density and Temperature

We used *Herschel* 160, 250, 350, and 500 μm observations of L1451 to derive the column density and temperature of the dust. There is no detectable emission at 70 μm toward this region. The *Herschel* images were corrected for the zero-level offset based on a comparison with *Planck* and DIRBE/IRAS data (Meisner & Finkbeiner 2015). In detail, we added offsets of 37.1, 42.6, 23.3 and 10.2 MJy/sr to the *Herschel* 160, 250, 350 and 500 μm maps, respectively. The images were convolved to the angular resolution of the *Herschel* 500 μm band ($\sim 36''$) using the convolution kernels from Aniano et al. (2011), and were regridded to a common pixel size of $10''$. The fitting was performed on a pixel-by-pixel basis with a modified blackbody spectrum of $I_\nu = \kappa_\nu B(\nu, T)\Sigma$, where κ_ν is the dust mass opacity coefficient at frequency ν , $B(\nu, T)$ is the Planck function at temperature T , and $\Sigma = \mu m_p N(H_2)$ is the gas mass column density for a mean molecular weight of $\mu = 2.8$ (e.g. Kauffmann et al. 2008) assuming a gas-to-dust ratio of 100:1. We assume $\kappa_\nu = 0.1 \times (\nu/10^{12} \text{ Hz})^\beta \text{ cm}^2 \text{ g}^{-1}$ (Beckwith & Sargent 1991) and $\beta = 1.7$.

The resulting column density and temperature maps are shown in Figures 13 and 14, respectively. We validated our SED fitting procedure by comparing our derived optical depth to that of the Planck Collaboration et al. (2014) model. Specifically, we re-ran our SED fits after smoothing the *Herschel* input maps to match the Planck Collaboration et al. (2014) resolution of $5'$, and found that our derived 300 μm optical depth agrees with that of the *Planck*-based model to within 5% on average. The mean column density of L1451 that is enclosed within the $2.0 \times 10^{21} \text{ cm}^{-2}$ contour in Figure 13 (the white contour that encircles all of the high column density regions) is $3.7 \times 10^{21} \text{ cm}^{-2}$ with a standard deviation of $1.7 \times 10^{21} \text{ cm}^{-2}$. The peak column density of $1.2 \times 10^{22} \text{ cm}^{-2}$ occurs at the location of the Bolocam source, PerBolo 4. The mean temperature within the 15.0 K contour of Figure 14 is 14.0 K, with a standard deviation of 0.7 K. A minimum temperature of 11.9 K occurs at the location of L1451-mm.

Gas kinetic temperature measurements exist toward the four Bolocam sources in our field (Rosolowsky et al. 2008a). Those gas temperatures are ~ 2 – 3.5 K lower than we find by fitting the *Herschel* SEDs. Our results, and those from Planck Collaboration et al. (2014) that we compared to, assume emission from a single cloud layer. However, variations in temperature along the line of sight, typically caused by a warmer layer of foreground and background material surrounding a dense, cold star-forming region, are often present. This warmer cloud component can drive the fitted temperature up and fitted column density down when only doing a single

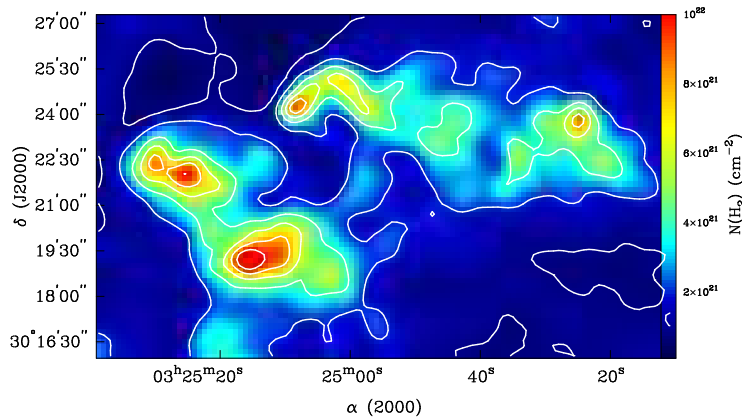


Fig. 13.— Column density map of L1451 derived from *Herschel* 160, 250, 350, and 500 μm data. The white contours correspond to $N(\text{H}_2)=[0.8, 2.0, 4.0, 6.0, 8.0, 10.0]\times 10^{21} \text{ cm}^{-2}$. The measured column densities toward the densest regions are likely systematically underestimated by a factor of two if considering two-temperature models over single-temperature models; see the discussion in the text.

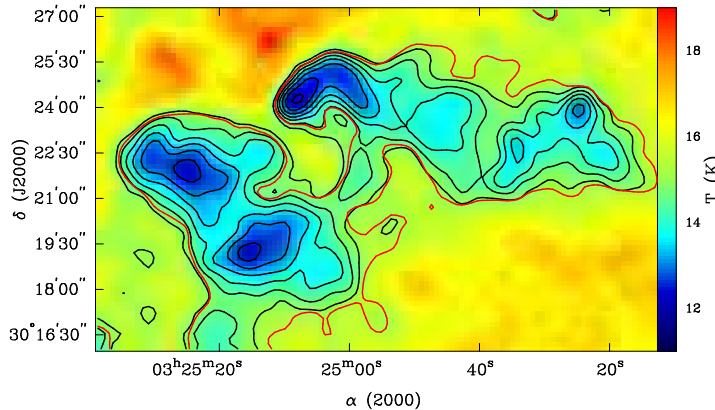


Fig. 14.— Temperature map of L1451 derived from *Herschel* 160, 250, 350, and 500 μm data. The black contours represent 12 to 15 K, in 0.5 K increments. The red contour represents a column density of $2.0\times 10^{21} \text{ cm}^{-2}$, for comparison to Figure 13. The temperatures toward the densest regions are likely overestimated by a few Kelvin if considering two-temperature models over single-temperature models; see text for discussion.

component fit.

To estimate the systematic overestimation of temperatures and underestimation of column densities toward the densest regions of clouds, we created a simple radiative transfer model with a cold layer at 9 K (representing L1451) between two warmer layers at 17 K (representing foreground and background cloud material). If the warm layers have A_V of 0.4, then the temperature in cold layer regions with $A_V \gtrsim 2$ is overestimated by $\sim 2.5\text{--}5.5$ K when using a single component fit (e.g., measure 12 K instead of the true 9 K). This matches the differences between our temperatures and the temperatures from the ammonia data. Furthermore, measured column density values of a cold, dense region are predicted to be a factor of two lower than the true values in regions where the warm layers have A_V of 0.4 and the cold layer has $A_V \gtrsim 2$. If the lower-resolution *Herschel* beam is not filled in regions of cold, dense gas, then this could further bias temperatures to be too warm, and column densities to be too low. In Section 8, we will discuss how these systematic uncertainties can affect our virial analysis results. An upcoming paper will present a detailed comparison of single-layer and multi-layer SED fitting across Perseus, quantifying the improvement that can be achieved for cold, dense regions when considering the hot, diffuse component along the line-of-sight.

7.2. Dendrogram Analysis of Dust

The column density results in the previous section are angular resolution limited compared to our CLASSy maps, so it is difficult to estimate the mass within the smallest molecular structures we identified using the dendrogram analysis in Section 6. Therefore, we take the approach of first defining structures based on the dust data here, and then using the kinematic information within those structures to explore energy balance in the next section.

We converted the N_{H_2} column density map to an extinction map using a conversion factor of $N_{\text{H}_2}/A_V = (1/2) \times 1.87 \times 10^{21} \text{ cm}^{-2} \text{ mag}^{-1}$ (Draine 2003). We then ran our non-binary dendrogram algorithm on the extinction map to define dust structures in the field. We used an rms and branching step of $0.2 A_V$, and required that local maxima peak at least $0.4 A_V$ above the merge level to be considered a real leaf. The algorithm identified 8 leaves and 6 branches in the region where we have molecular line data.

The extinction map, with dendrogram-identified structures, is shown in Figure 15. Properties of the dendrogram structures are listed in Table 8, including their coordinate, size, weighted mean temperature and column density, and total mass. The mean temperature and column density, and total mass of each structure considers all of the emission interior to the structure (e.g., branch 9 includes emission from branch 9 and leaves 0 and 2). To calculate the total mass within each structure, we first converted the column density at each pixel to a solar mass unit as:

$$M(\alpha, \delta) = \mu_{\text{H}_2} m_H N_{\text{H}_2}(\alpha, \delta) A, \quad (1)$$

where μ_{H_2} is the molecular weight per hydrogen molecule (2.8), m_H is the mass of a hydrogen atom, $N_{\text{H}_2}(\alpha, \delta)$ is the column density at a pixel location, and A is the pixel area. As before, the assumed distance is 235 pc. We then totaled the mass enclosed within each structure. The mass of leaves ranges from 0.2 to $5.1 M_\odot$, and the mass enclosed within branches ranges from 3.0 to $15.9 M_\odot$. The mass interior to the yellow and purple contours in Figure 15 is $14.9 M_\odot$ and $12.4 M_\odot$, respectively.

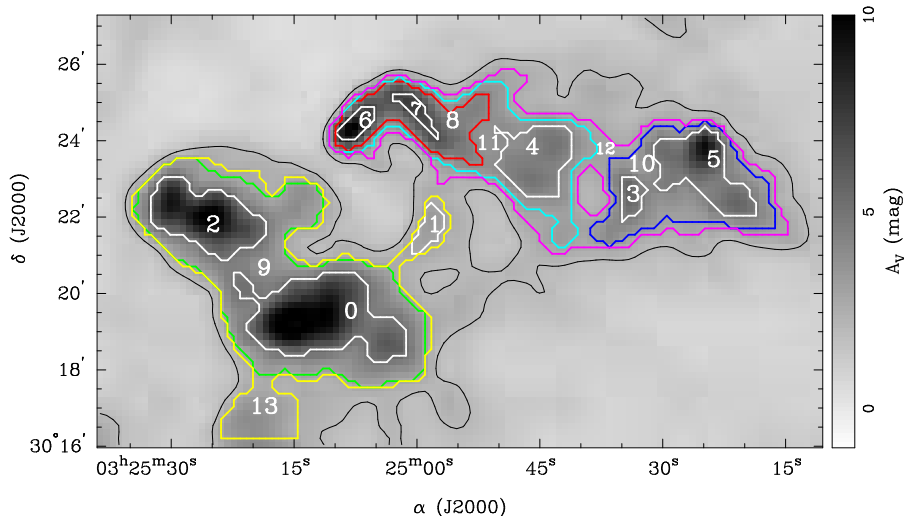


Fig. 15.— Visual extinction map of L1451 (greyscale), as derived from the column density map in Figure 13. The solid black contour represents $A_V = 2$, and the mean extinction within that contour is 3.8 mag with a 1.8 mag standard deviation. Dendrogram-derived dust structure boundaries are shown with colored contours. The peak extinction is ~ 13 mag within structure 0.

Table 8. Dust Structure Properties

No.	RA	DEC	Size	$\langle T \rangle$	$\langle N_{H_2} \rangle$	M_{tot}	$\sigma_{\text{tot}, N_2H^+}$	$\sigma_{\text{tot}, HCN}$	$\sigma_{\text{tot}, HCO^+}$
(1)	(h:m:s) (2)	(°:′:″) (3)	(pc) (4)	(K) (5)	(10^{21} cm^{-2}) (6)	(solar) (7)	(km s^{-1}) (8)	(km s^{-1}) (9)	(km s^{-1}) (10)
Leaves									
0	03:25:13.3	+30:19:05.8	0.23	13.6	5.1	5.1	0.34	0.39	0.49
1	03:25:00.2	+30:21:22.1	0.08	14.4	2.8	0.2	...	0.41	0.44
2	03:25:27.2	+30:21:43.6	0.17	13.2	5.0	3.1	0.27	0.29	0.40
3	03:24:35.5	+30:22:09.5	0.07	13.6	4.4	0.4	0.37	0.34	0.49
4	03:24:47.0	+30:23:11.2	0.14	13.9	4.0	1.4	...	0.54	0.64
5	03:24:26.8	+30:22:47.7	0.17	13.9	4.6	2.0	0.28	0.44	0.53
6 ^a	03:25:08.7	+30:24:09.5	0.07	12.2	7.2	0.5	0.25	0.25	0.33
7	03:25:01.5	+30:24:27.9	0.07	12.7	6.4	0.5	0.26	0.28	0.40
Branches									
8	03:25:01.5	+30:24:12.9	0.21	13.7	4.1	3.0	0.33	0.33	0.42
9	03:25:17.8	+30:20:07.0	0.41	14.2	3.1	13.1	0.44	0.47	0.54
10	03:24:29.2	+30:22:26.8	0.27	14.2	3.6	4.5	0.35	0.45	0.57
11	03:24:54.2	+30:23:38.9	0.33	14.1	3.3	6.2	0.34	0.39	0.51
12	03:24:43.1	+30:23:04.4	0.46	14.3	3.1	12.4	0.39	0.43	0.54
13	03:25:17.1	+30:19:52.8	0.51	14.3	3.0	14.9	0.47	0.50	0.56

Note. — (4) Geometric mean of major and minor axis fit to structure (used as diameter of structure). (5) Weighted mean temperature within structure. (6) Weighted mean column density of H_2 within structure. (7) Total mass within structure. (8) N_2H^+ velocity dispersion calculated from integrated spectrum across structure; see Section 8.2 for discussion. (9) HCN velocity dispersion calculated from integrated spectrum across structure; see Section 8.2 for discussion. (10) HCO^+ velocity dispersion calculated from integrated spectrum across structure; see Section 8.2 for discussion. ^a L1451-mm is located within this structure.

8. Discussion

The goal of this discussion section is to understand the state of star formation in L1451 using results and analysis presented in previous sections. We selected L1451 as a CLASSy region because of its very low star formation activity. There are no confirmed protostar detections, and only one confirmed compact continuum core. This is very different from the other CLASSy regions, which have many protostars and outflows. We wanted to use L1451 to study the structure and kinematics of the densest regions of clouds before star formation activity feeds back into the cloud.

We now explore the following questions. What column density threshold are we capturing with our spectral line observations, and do dendrogram-identified structures trace actual column density features that can inform structure formation in a young cloud? If so, will any structures go on to form stars? We address these questions in this section by exploring the correspondence between molecular line and continuum emission, with a virial analysis of L1451 structures, and by describing the similarities and differences between L1451-mm and L1451-west. We conclude with an analysis of the three-dimensional morphology of L1451 on the largest scales to see how it compares to more evolved CLASSy regions.

8.1. Connecting molecular and column density structures

L1451 is the one CLASSy region with strong, widespread HCO^+ and HCN that is not affected by outflows and significant self-absorption. This enabled a dendrogram analysis of all three molecules in Section 6, instead of just N_2H^+ , and lets us now compare the identified molecular structures to the column density structure of L1451 presented in Section 7. Figures 16 and 17 have the dendrogram footprints of the lowest-level branches, and all the leaves, respectively, overplotted on column density structure derived from *Herschel* data. We combined the footprints of all the contoured emission in Figures 16 and 17 to create a mask for the column density map for determining how well the molecular emission captures material at different column densities.

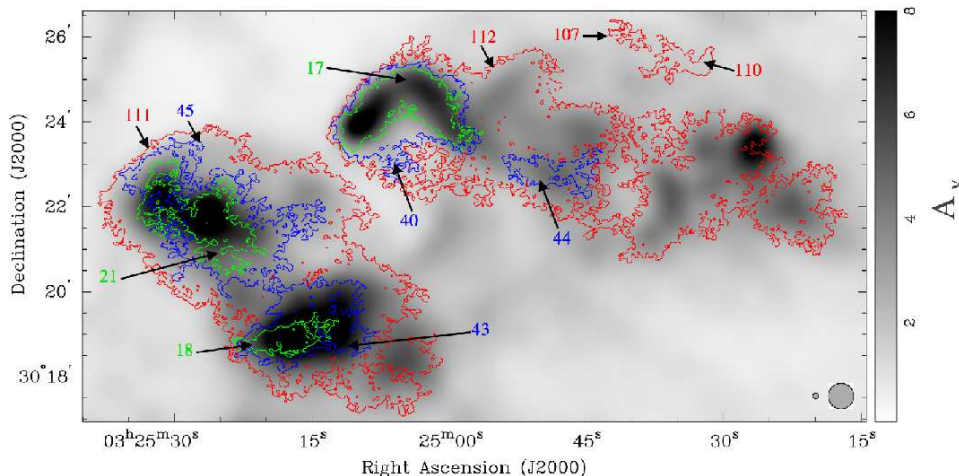


Fig. 16.— Dendrogram lowest-level branch footprints for all molecules, overplotted on our extinction map that was regridded to match the CLASSy pixel scale (beams for column density ($36''$) and molecular ($8''$) maps are in the lower right). Red = HCO^+ , blue = HCN , and green = N_2H^+ . We label each branch with its dendrogram structure number, and branch properties can be examined in Tables 4–6.

Figure 18 shows cumulative distribution functions for column density in regions with and without line emission (regions with line emission are defined as having at least a single molecular detection, while regions without line emission are defined as having no molecular detections). A threshold for star formation above

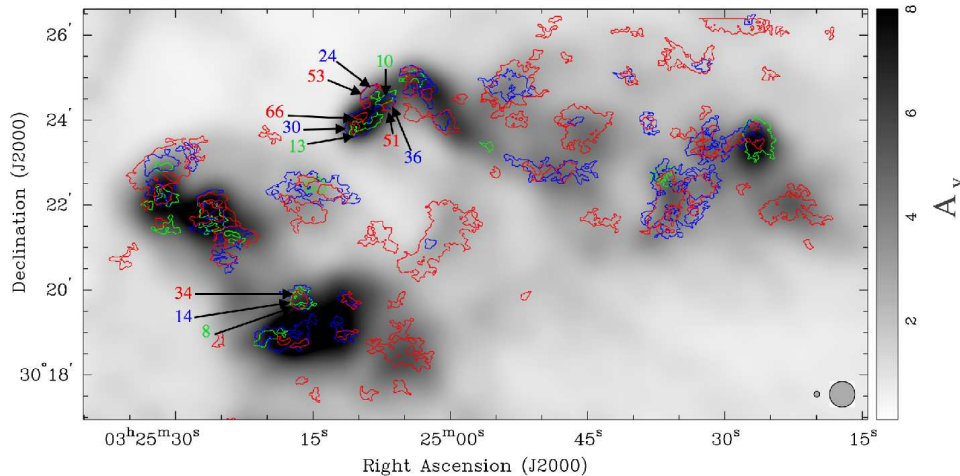


Fig. 17.— Dendrogram leaf footprints for all molecules, overplotted on our extinction map that was regridded to match the CLASSy pixel scale (beams for column density ($36''$) and molecular ($8''$) maps are in the lower right). Red = HCO^+ , blue = HCN , and green = N_2H^+ . We label a few examples with dendrogram structure numbers, and leaf properties can be examined in Tables 4–6.

$A_V \sim 8$, or an H_2 column density of $7.5 \times 10^{21} \text{ cm}^{-2}$, has been postulated based on the distribution of prestellar cores and protostars within the densest regions of molecular clouds (Johnstone et al. 2004; Hatchell et al. 2005; André et al. 2014, and references therein). Only 0.002% of dust regions without a molecular gas detection are above the threshold column density if we take our derived column densities as correct. If our measured column densities are uniformly underestimated by a factor of two from the true values, as was discussed in Section 7.1, still only 1% of dust regions without a molecular gas detection are above the threshold column density. 90% of the regions where we detect molecules are at column densities above $1.9 \times 10^{21} \text{ cm}^{-2}$, with a maximum of $1.3 \times 10^{22} \text{ cm}^{-2}$, and minimum of $8.9 \times 10^{20} \text{ cm}^{-2}$. 90% of the regions where we do not detect molecules are below $2.4 \times 10^{21} \text{ cm}^{-2}$, with a maximum of $7.8 \times 10^{21} \text{ cm}^{-2}$, and minimum of $3.6 \times 10^{20} \text{ cm}^{-2}$. This shows that spectral line observations using our suite of dense-gas tracer molecules are a great probe of the star forming material in young regions above the threshold for star formation and down to column densities of a few $\times 10^{21} \text{ cm}^{-2}$.

This result of molecular emission capturing most of the cloud material near and above the threshold of star formation, combined with the result that the branches in Figure 16 are fragmenting to form the leaves in Figure 17 in a similar hierarchical fashion for each molecule (see Section 6.3), suggests that dendrogram-identified molecular structure is able to trace physical structure formation, despite some biases due to chemistry and extinction. This provides observational evidence that structure formation precedes star formation in molecular clouds. Complex morphological structure in a turbulent cloud can be formed by turbulence-driven cascades from large-scale flows before the onset of star formation (Klessen & Hennebelle 2010, and reference therein), and it can be produced from internally-driven turbulence from protostellar feedback (Carroll et al. 2009; Federrath et al. 2014; Nakamura & Li 2014). Our result helps to disentangle externally and internally driven structure, which it is important for demonstrating an observational case of complex, hierarchical dense gas structure existing in a turbulent cloud at an epoch before internal feedback can impact the natal cloud environment.

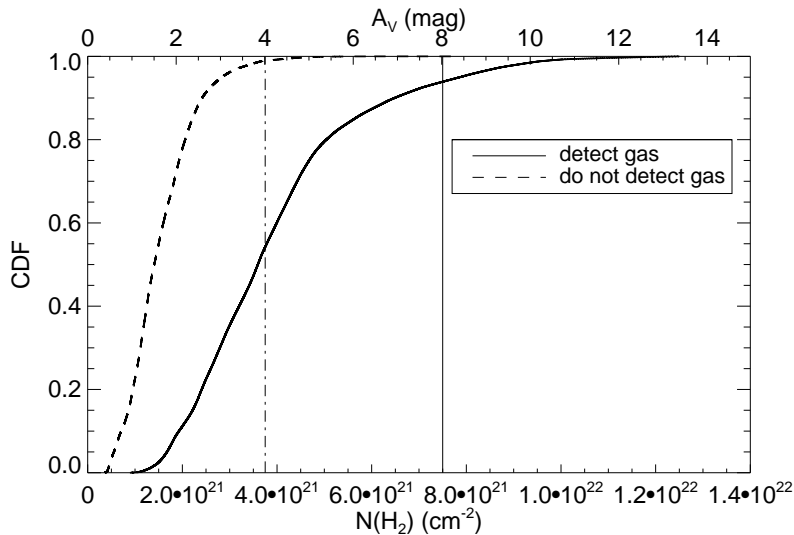


Fig. 18.— Cumulative distribution functions for the areas of the L1451 column density map where we have detected molecular emission (solid curve), and the areas where we have not detected molecular emission (dashed curve). The solid vertical line marks the column density threshold for star formation (André et al. 2014, and references therein), while the dashed-dotted vertical line represents that threshold if our measured column densities are underestimated by a factor of two from the true column densities.

8.2. Virial Analysis of Structures

We next use a virial analysis to assess the stability of L1451 structures against collapse. We know one star is currently forming in L1451, based on the detection of compact 3 mm emission at L1451-mm. However, it is unknown if the majority of L1451 structures are dominated by gravitational potential energy and therefore unstable against collapse, or rather dominated by internal pressure and therefore stable against collapse and possibly confined by large external pressure. For the virial analysis, we use the dust results in combination with the molecular data. In Section 7, we derived column densities and temperatures across L1451 at the angular resolution of the longest wavelength *Herschel* band (36"). We also found dendrogram-identified dust structures in the extinction map. In this section, we use that information for dust leaves along with CLASSy kinematic data from Section 5 to assess the energy balance of several structures in L1451.

The virial theorem is useful for describing the stability of structures. There are several approaches for applying the virial theorem to molecular cloud observations in the literature (e.g., Larson 1981; Bertoldi & McKee 1992; McKee & Zweibel 1992; Ballesteros-Paredes 2006; Kauffmann et al. 2013). We follow the formalism of Bertoldi & McKee (1992) and Kauffmann et al. (2013), who define the observed virial parameter of an individual structures as

$$\alpha_{obs} \equiv \frac{5\sigma_{tot}^2 R}{GM} \quad (2)$$

where σ_{tot} , R , and M are the one-dimensional velocity dispersion (including thermal and non-thermal gas motions), radius, and mass of the structure, respectively. Kauffmann et al. (2013) summarize that the critical value of the virial parameter for a spherical structure not supported by magnetic pressure is $\alpha \approx 2$. Structures with $\alpha \ll 2$ are supercritical and unstable against collapse unless they are supported by magnetic fields. Structures with $\alpha \gg 2$ are subcritical and stable against collapse—they should dissipate unless they are confined by high external pressure. As discussed in Kauffmann et al. (2013), this critical value includes the effects of density gradients within and outside of the structure, as well as surface pressure from the immediate surrounding medium.

For the virial parameter definition in Equation 2, M is the mass of each source derived from our *Herschel* analysis and is reported in Column 7 of Table 8. A major source of systematic uncertainty in the calculated mass is the underestimate in the column density value derived from the *Herschel* SED fitting in Section 7.1. In Section 7.1, we discussed how using a single temperature model (ignoring the warmer foreground and background component surrounding the colder L1451 region) for fitting the *Herschel* SEDs leads to estimated column densities that are about a factor of two lower than the true column densities. If the measured column densities are a factor of two lower than the true column densities, this directly leads to a mass underestimate by a factor of two and a virial parameter overestimate by a factor of two. Work has been done on the galactic scale to estimate dust mass underestimation due to poor spatial resolution and temperature mixing in *Herschel* data. For example, Galliano et al. (2011) found that *Herschel*-derived dust masses can be $\sim 50\%$ underestimated in the Large Magellanic Cloud (LMC). Even though our observations have much higher spatial resolution than observations of the LMC, this is a useful comparison since the warm-cold temperature contrast in local clouds like L1451 may be more extreme than on galactic scales. For core scales, Shetty et al. (2009) demonstrated that temperature variations along the line-of-sight will lead to inaccurate measurements of dust properties from SED fitting. We will consider the likely systematic underestimation of mass from our SED fitting in the discussion of results below.

The radius of each structure, R , in the virial parameter definition is half of the size reported in Column 4 of Table 8. The one-dimensional velocity dispersion of each structure, σ_{tot} , in the virial parameter definition includes thermal and non-thermal support against collapse. The thermal component of the velocity dispersion was calculated as:

$$\sigma_{th} = \sqrt{\frac{kT}{\mu m_H}}, \quad (3)$$

where T is the mean temperature of the dust within the structure, μ is the mean molecular weight (2.33), and m_H is the hydrogen atomic mass. The non-thermal component of the velocity dispersion was calculated for each molecular tracer separately, as:

$$\sigma_{nth,tracer} = \sqrt{\sigma_{obs,tracer}^2 - \sigma_{th,tracer}^2} \quad (4)$$

where $\sigma_{obs,tracer}^2$ is the observed velocity dispersion of the molecular emission within the structure, and $\sigma_{th,tracer}$ is the thermal velocity dispersion of the molecule at the mean temperature found within the structure:

$$\sigma_{th,tracer} = \sqrt{\frac{kT}{\mu_{tracer} m_H}}. \quad (5)$$

We determined $\sigma_{obs,tracer}^2$ by masking the CLASSy molecular data cubes using the boundaries of each dust structure, generating an integrated spectrum for each molecule, and fitting for the velocity dispersion of that integrated spectrum. The final $\sigma_{total,tracer}$ value was then calculated as:

$$\sigma_{tot,tracer} = \sqrt{\sigma_{th}^2 + \sigma_{nth,tracer}^2} \quad (6)$$

and is reported in Columns 8, 9, and 10 of Table 8 for N_2H^+ , HCN, and HCO^+ , respectively. The temperature overestimate from the single-temperature *Herschel* SED fitting discussed in Section 7.1 systematically increases the thermal component of the internal velocity dispersion of each structure, thereby increasing the dispersive term used to calculate α . The temperature error is less significant than the factor of two column density error discussed above, but still contributes a $\sim 7\%$ systematic increase in the virial parameter if the measured temperature is overestimated by 2.5 K from the true value.

Virial parameters for each dust leaf structure are reported in Table 9, with unique values for each molecular tracer resulting from different velocity dispersions between the tracers. For each tracer, we first report the

measured virial parameter using the masses derived from the *Herschel* SED fitting, and then report a value reduced by a factor of two to account for the likely systematic underestimation of the fitted column density values discussed above.

Two things are clear from the α values in Table 9. First, the α values typically vary by a factor of two between tracers, with N_2H^+ and HCO^+ data giving the lowest and highest virial parameter, respectively. This trend with molecular tracer is not surprising, since it connects to the differences in spatial extent and kinematics between molecular emission discussed in Sections 4 and 5. The HCO^+ traces the most spatially extended emission on the plane of the sky, implying it is tracing the most extended emission along the line-of-sight if the two spatial directions are correlated. This implication is strongly supported by HCO^+ having the largest line-of-sight velocity dispersions. Since the virial parameter scales as the square of the velocity dispersion of each molecule, the larger HCO^+ velocity dispersion leads to the larger virial parameter. This shows that the choice of kinematic tracer has large impact on the interpretation of a given structure.

Second, all virial parameter values are greater than two if we use the masses derived from the single-temperature model of *Herschel* SED fitting. If we assume that the mass is underestimated by a factor of two and the virial parameter is overestimated by a factor of two (ignoring the systematic temperature uncertainty also increasing the virial parameter), then some of the structures have virial parameters near or less than the critical value of 2 for instability against collapse. Structures 1, 3, 4, and 7 have α above two regardless of the molecular tracer used or assumption of mass. These structures have the weakest dense gas emission in the field and/or appear the least centrally condensed in the column density maps, so it is reasonable that they appear to be the least unstable against collapse. Structures 0, 2, 5, and 6 have α near or below two, appear centrally condensed in the column density map, and have strong molecular emission in the line maps. Structure 0 contains Per Bolo 4, structure 2 contains Per Bolo 6, structure 5 contains L1451-west, and structure 6 contains L1451-mm. These results together support these structures (or at least the central parts of these structures) being unstable against collapse, and the L1451 region as a whole being at the onset of forming a few protostars.

We will extend this type of virial analysis in upcoming work to compare virial parameters across CLASSy regions. This way, even if there are systematic and statistical uncertainties, all structures will have been observed and analyzed in the same way, making a relative comparison of virial parameters across cloud regions at different stages of evolution possible.

Table 9. Virial Parameters

No.	α (N_2H^+)		α (HCN)		α (HCO^+)	
	1-temp	2-temp ^a	1-temp	2-temp ^a	1-temp	2-temp ^a
(1)	(2)	(3)	(4)	(5)	(6)	(7)
0	3.0	1.5	4.0	2.0	6.1	3.1
1	28.5	14.3	32.9	16.5
2	2.3	1.2	2.8	1.4	5.2	2.6
3	15.3	7.7	13.1	6.6	26.0	13.0
4	17.5	8.8	24.8	12.4
5	3.8	1.9	9.3	4.7	13.5	6.8
6 ^b	4.4	2.2	4.5	2.3	7.9	4.0
7	6.2	3.1	6.8	3.4	14.0	7.0

Note. — (1) Leaf number from Table 8. (2) Virial parameter calculated using Equation 2 with the N_2H^+ velocity dispersion and mass derived from *Herschel* single-temperature SED fitting. (3) Column 2, corrected by a factor of two to account for the likely underestimation of column density (and therefore mass) from single-temperature SED fitting discussed in text. (4) Same as Column 2, but using the HCN velocity dispersion. (5) Same as Column 3, but using the HCN velocity dispersion. (6) Same as Column 2, but using the HCO^+ velocity dispersion. (7) Same as Column 3, but using the HCO^+ velocity dispersion. ^aWe are not formally using a two-temperature model to fit the *Herschel* SEDs, but are applying a correction factor that estimates the likely effect of using such a model. ^bL1451-mm is located within this structure.

8.3. Closer Look at L1451-mm and L1451-west

In this section, we explore the properties of the two centrally condensed, roughly spherical cores in L1451. One is L1451-mm, which we know is a compact object containing a YSO or a FHSC (Pineda et al. 2011). The other is L1451-west, which has been discovered with these observations. We summarize the morphology and kinematics of L1451-mm below, and then describe the properties of L1451-west and how they compare to L1451-mm.

The top row of Figure 19 shows molecular and continuum features of L1451-mm. L1451-mm is the only confirmed compact continuum core in L1451, and all molecules trace strong emission near, and surrounding its location. All molecules peak in integrated emission at a location slightly offset from the L1451-mm compact continuum core. The molecular emission that surrounds the core is more concentrated for N_2H^+ , and more widespread for HCN and HCO^+ . The N_2H^+ centroid velocity field shows a gradient across the core, which Pineda et al. (2011) modeled as a rotating and infalling envelope using slightly higher angular resolution ($5''$) data; we measure a gradient of about $6 \text{ km s}^{-1} \text{ pc}^{-1}$ through the peak of integrated emission at a position angle of 120 deg east of north (see white line in the top row panels of Figure 19). The velocity dispersion field is narrowest around the edges of the core with minima $\sim 0.07 \text{ km s}^{-1}$, and it shows an increase toward the core location, with a peak $\sim 0.2 \text{ km s}^{-1}$. See Pineda et al. (2011) for detailed discussion and modeling of the possibility that L1451-mm is a dense core with a central YSO and disk, or a dense core with a central FHSC.

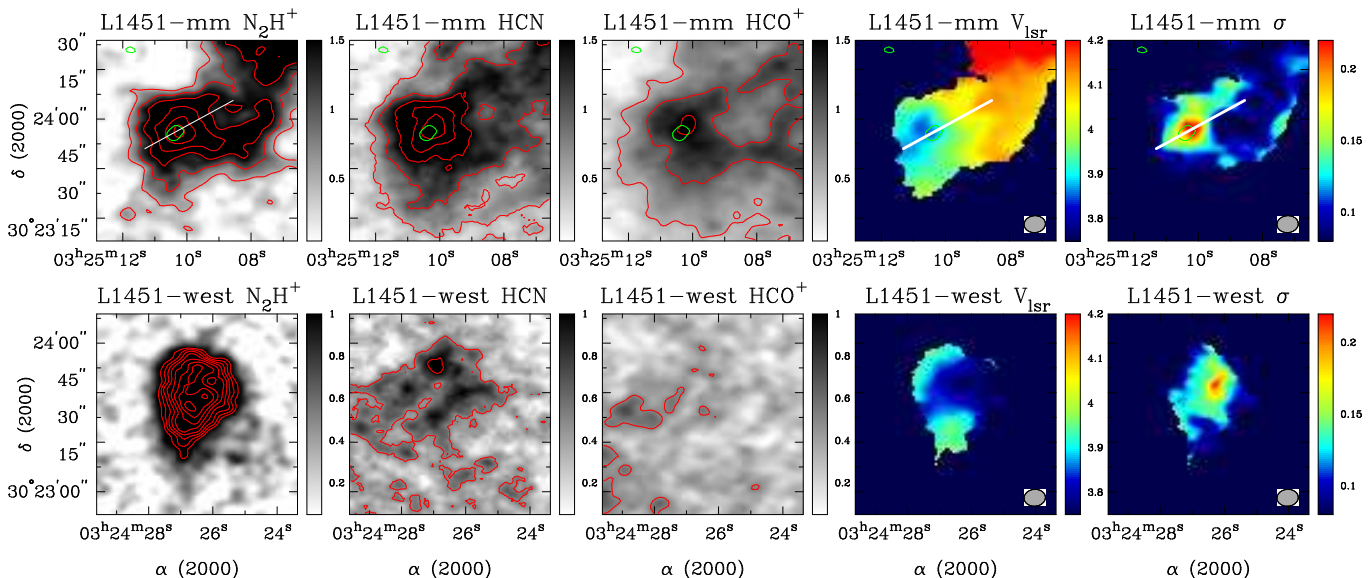


Fig. 19.— The top and bottom rows show properties of L1451-mm and L1451-west, respectively. From left-to-right, the panels are: N_2H^+ , HCN, and HCO^+ integrated intensity ($\text{Jy beam}^{-1} \text{ km s}^{-1}$), N_2H^+ centroid velocity (km s^{-1}), and N_2H^+ velocity dispersion (km s^{-1}). The kinematic maps of each source are on the same color scale. The velocity dispersion is expressed as Gaussian σ (FWHM/2.355 in km s^{-1}). The green $0.0039 \text{ mJy beam}^{-1}$ contour represents our L1451-mm compact continuum detection. The red contours are used to accentuate specific features in the greyscale maps. The white lines represent the direction of the measured velocity gradient through L1451-mm.

The bottom row of Figure 19 shows molecular and continuum features of L1451-west. The N_2H^+ integrated intensity map does not have a single peak of integrated emission at the center of the structure. Instead, there are two peaks in the southern half of the source $\sim 2.5 \text{ Jy beam}^{-1} \text{ km s}^{-1}$, and one peak in the northern half of the source $\sim 2.4 \text{ Jy beam}^{-1} \text{ km s}^{-1}$ (the red contours in the bottom-left panel of Figure 19 represent 1.1 – $2.5 \text{ Jy beam}^{-1} \text{ km s}^{-1}$ in $0.2 \text{ Jy beam}^{-1} \text{ km s}^{-1}$ increments). The source is considerably weaker in HCN, and not detected in HCO^+ . This apparent lower-abundance of HCO^+ may indicate that this might be a very cold, dense region of L1451, where CO is depleted. If CO is frozen out onto dust grains, then it is not able to destroy

N_2H^+ , and N_2H^+ remains abundant. Likewise, if CO is frozen out, it is not available to create HCO^+ through collisions with H_3^+ (Prasad & Huntress 1980). Our temperature map in Figure 14 does not suggest that dust around L1451-west is significantly colder than L1451-mm, but higher-resolution continuum observations with modeling to remove any warm component could reveal differences in the two sources that are not resolvable with the current data. It is also possible that the HCO^+ ($J = 1 \rightarrow 0$) photons are being absorbed by HCO^+ molecules in lower-density foreground gas; observations of higher- J transitions are needed to test this.

The N_2H^+ centroid velocity field of L1451-west shows a relatively complex structure compared with L1451-mm, with higher velocity emission in the southern and northeastern sections of the core, and lower velocity emission toward the center and west of the core. The velocity dispersion field of L1451-west is narrowest around the edges of the core with minima $\sim 0.07 \text{ km s}^{-1}$, and it peaks near $\sim 0.2 \text{ km s}^{-1}$ at the location of lowest velocity emission in the central part of the source. It is possible that infall is producing the increased velocity dispersion, in addition to any undetected outflows and/or unresolved disk rotation from source center. Infall would broaden the molecular emission toward the core center, with the blueshifted emission being brighter than the redshifted emission if the N_2H^+ emission is optically thick. This could explain why the peak of velocity dispersion is at the location with the bluest centroid velocity. The signal-to-noise of the detectable HCN spectra are too low to look for evidence of infall motions, so this needs to be followed up with deeper observations of optically thick and thin lines.

There is no compact continuum emission detected toward L1451-west. The 3σ flux density limit for a point source ($\lesssim 3'' = 700 \text{ AU}$) in our observations is 3.9 mJy, corresponding to a mass limit of $0.08 M_\odot$ for the conversion from mJy to M_\odot discussed in Paper I. We use the location of peak velocity dispersion as a proxy for the location of a compact continuum core, if it exists; this peak is offset from the peak in the *Herschel*-derived column density map by about $16''$.

We estimated the size and physical density of L1451-mm and L1451-west for a more detailed comparison. To determine the size, we used the MIRIAD `imfit` routine to fit a two-dimensional Gaussian to the N_2H^+ integrated intensity map. The geometric means of the major and minor axes are $37''$ and $32''$ for L1451-mm and L1451-west, respectively. To determine the maximum physical density, we took the peak column density of each source within the fitted Gaussian, and assumed their depth was the same extent as their geometric mean across the plane of the sky. For both sources, the physical density is $7\text{--}8 \times 10^4 \text{ cm}^{-3}$ in the $8''$ beam. This density is sensible, considering that we observe N_2H^+ and HCN ($J = 1 \rightarrow 0$) in L1451, which are molecular transitions with effective excitation densities on the order of 10^5 cm^{-3} .

We also compared the mass within 4200 AU ($18''$ at $d=235 \text{ pc}$) to the intrinsic radius at 70% of peak intensity, following the analysis of starless cores presented in Kauffmann et al. (2008). We measured the mass using the *Herschel* data, and got 0.22 and $0.23 M_\odot$ for L1451-mm and L1451-west, respectively. We measured the radius using the N_2H^+ integrated intensity, since the dust data is not as well resolved to derive accurate radius measurements. L1451-mm measured $8''$, and L1451-west measured $12''$ at 70% of the peak intensity. Compared to the sample of starless cores in Kauffmann et al. (2008), L1451-mm is more centrally dense than most starless objects, while L1451-west is near the upper limit of central density seen in starless objects.

All of these observational results point to L1451-west being similar to, but slightly less evolved than, L1451-mm, yet more evolved than a prestellar core. Although deep continuum and spectral line observations will be needed to determine the true nature of these sources, they are some of the best evidence that L1451 is a region that is just starting to form its first stars.

8.4. Three-Dimensional Morphology of L1451

Comparing the projected size of cloud structure to its depth along the line-of-sight gives a better understanding of the three-dimensional geometry of a region where stars are forming (e.g., a region that is primarily

planar/sheet-like versus one that is more spherical). We described a statistical method to estimate the typical line-of-sight depth of cloud structures in Paper I. The method uses the spatial and kinematic properties of dendrogram objects presented in Tables 4–6. It assumes that the V_{lsr} variation (ΔV_{lsr} ; Column 11) of a structure scales with its projected size (Column 9) in a turbulent medium. It also assumes that the mean non-thermal velocity dispersion ($\langle\sigma\rangle_{\text{nt}}$) of a dendrogram structure scales with its depth along the line-of-sight in a turbulent medium. We calculate $\langle\sigma\rangle_{\text{nt}}$ for each structure in all three molecular tracers by subtracting the thermal velocity dispersion of 10 K gas of the given tracer from the value reported in Column 12 of Tables 4–6: $\langle\sigma\rangle_{\text{nt}} = \sqrt{\langle\sigma\rangle^2 - \sigma_{\text{th}}^2}$. With those assumptions, we create two size-linewidth relations using all the dendrogram structures (one with projected size versus $\langle\sigma\rangle_{\text{nt}}$, and the other with projected size versus ΔV_{lsr}), and take the spatial scale where they cross as the typical depth of the region. See Paper I for the theoretical framework and numerical results that justify this method.

We used the method in previous papers to argue that the typical depth of the N_2H^+ emission in the CLASSy Barnard 1 and Serpens Main regions was 0.1–0.2 pc (see Paper I and Lee et al. (2014)). Figure 20 shows the size-linewidth relations for each molecule. As in the analysis of Barnard 1 in Paper I and Serpens Main in Lee et al. (2014), the projected size- ΔV_{lsr} for each molecule has a positive slope (which is expected for a turbulent medium), while the projected size- $\langle\sigma\rangle_{\text{nt}}$ relationship has a flatter slope (which is expected if all structures have a similar depth along the line-of-sight, independent of their projected size). The best-fit lines to the relations cross at a size-scale of 0.11 and 0.10 pc for N_2H^+ and HCN, respectively, indicating that those molecules are tracing structures ~ 0.1 pc in depth. The HCO^+ fits cross near 0.40 pc, indicating that it is tracing structures with larger line-of-sight depths compared to the other molecules. This is consistent with HCO^+ detecting larger-scale, lower density gas than the other molecules.

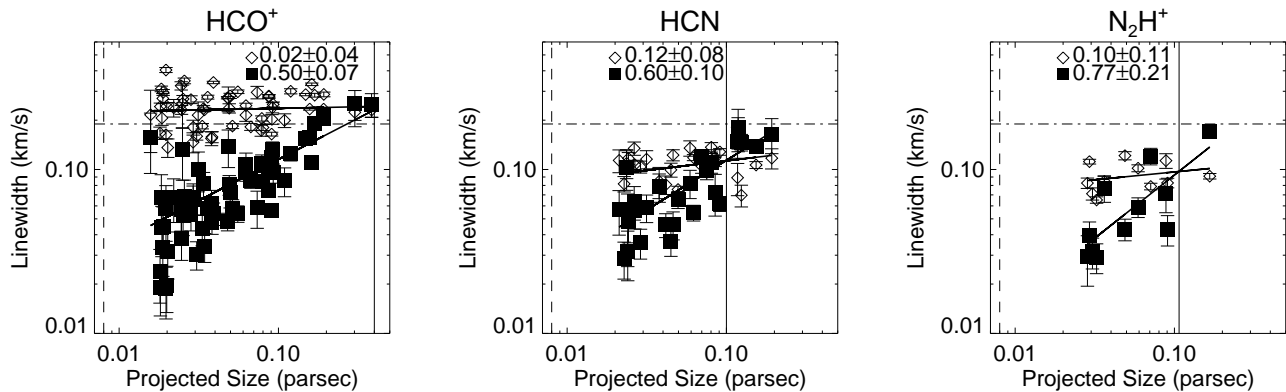


Fig. 20.— Scaling relations between projected structure size and V_{lsr} variation (ΔV_{lsr} ; solid squares), and projected structure size and mean non-thermal velocity dispersion ($\langle\sigma\rangle_{\text{nt}}$; open diamonds), for each molecule. The solid lines represent single power-law fits to the data points. The horizontal line represents the typical thermal speed for H_2 at gas kinetic temperatures near 10 K. The vertical dashed line represents our spatial resolution of ~ 0.008 pc. The vertical solid line represents the spatial scale where the power-law fits intersect.

These results show that the N_2H^+ emission in L1451 has similar depth as it does in Barnard 1 and Serpens Main. However, there are differences between L1451 and the other regions that lead us to different conclusions about the large-scale structure of L1451. In Paper I, we said that the depth of Barnard 1 (0.1–0.2 pc) is comparable to the largest size of individual N_2H^+ dendrogram structures identified from the isolated N_2H^+ hyperfine component (0.2–0.3 pc). But we followed up by discussing how the Barnard 1 has contiguous N_2H^+ structure at parsec-scales when considering the full N_2H^+ emission instead of just the isolated hyperfine component. We used the estimated 0.1–0.2 pc depth and observed parsec projected size of Barnard 1 to conclude that the region is flattened at the largest detectable scales.

In projection, the full N_2H^+ emission, sub-millimeter continuum emission, and other molecular emission from L1451 region does not appear to have contiguous structure across parsec scales like all other CLASSy regions. Instead, the emission is concentrated in a few major features, sub-parsec in size, that were identified in Section 4. Because of this, we argue that the L1451 is not a flattened, sheet-like region of dense gas and dust at parsec-scales with connected substructure. In N_2H^+ , it appears more like a loose collection of dense concentrations that are ~ 0.2 pc projected on the sky and ~ 0.1 pc deep.

The physical density of the regions of L1451 with N_2H^+ emission can be estimated from the cloud depth and column density. For a 0.1 pc depth of N_2H^+ emission and a mean $\text{N}(\text{H}_2)$ of $6 \times 10^{21} \text{ cm}^{-2}$ measured from the *Herschel* data, the derived physical density is $2 \times 10^4 \text{ cm}^{-3}$ in the regions of L1451 with N_2H^+ emission. It is possible to excite N_2H^+ at a range of physical densities, where the range depends on the molecular column density (and thus relative abundance of N_2H^+ to H_2), the gas kinetic temperature, and the linewidth of emission. Using the RADEX program (van der Tak et al. 2007), we find that N_2H^+ ($J = 1 \rightarrow 0$) can reach 1 K brightness temperatures with a physical density of $2.7 \times 10^4 \text{ cm}^{-3}$ if the gas kinetic temperature is 12 K, the molecular column density of N_2H^+ is $6 \times 10^{12} \text{ cm}^{-2}$, and the linewidth of emission is 0.3 km s^{-1} . This physical density is essentially the same as derived from our depth and column density measurements, providing a consistency check to our measurements.

We can compare the typical depth of the molecular emission to the projected size of the largest-scale structures of each molecule in Figure 16 to infer the three-dimensional morphology of the individual molecular structures. The projected size of N_2H^+ structure 21 (lowest level branch of Features A) is ~ 0.17 pc, structure 18 (lowest level branch of Features C) is ~ 0.09 pc, and structure 17 (lowest level branch of Features B) is ~ 0.17 pc. For a typical N_2H^+ depth of 0.11 pc, these structures have axis ratios of 1.5:1 and 0.8:1, with a mean of 1.3:1. The projected size of HCN structure 45 (lowest level branch of Feature A) is ~ 0.24 pc, structure 43 (lowest level branch of Feature C) is ~ 0.17 pc, and structure 40 (lowest level branch of Feature B) is ~ 0.19 pc. For a typical HCN depth of 0.10 pc, these structures have axis ratios between 2.4:1 and 1.7:1, with a mean axis ratio of 2.0:1. The projected size of HCO^+ structure 111 (lowest level branch connecting Features A and C) is ~ 0.43 pc, and structure 112 (lowest level branch connecting Features B, H, F, G, E, and I) is ~ 0.46 pc. For our derived typical HCO^+ depth of 0.40 pc, these structures have axis ratios of 1.1:1 and 1.2:1.

With axis ratios between 0.8:1 and 2.4:1 for individual structures that do not connect at larger scales, these results support the L1451 region being composed of discrete, high-density structures that are approximated as ellipsoids. In addition to not having contiguous, flattened structure at parsec scales like the other CLASSy regions studied to-date (Serpens Main and Barnard 1), none of the large-scale structures of L1451 appear to have clear filamentary substructure like was the case in all other CLASSy regions. These results differentiate L1451 from the other regions in a way beyond the lack of protostars and outflows.

If L1451 is not a flattened, sheet-like region at parsec-scales, if it does not have prominent filamentary structure, and if it has less active star formation than the other CLASSy regions, then it is natural to speculate what caused these differences. A cloud complex, like Perseus, that spans tens of parsecs will have different turbulent energies in different parts of the cloud. Simulations of turbulence-driven star formation with supersonic turbulence (e.g., Federrath & Klessen 2012) show that star formation within several-parsec scale clouds is clustered in regions where material has been compressed to high densities, leaving voids of star formation in other parts of the cloud. We speculate that the L1451 region of Perseus may not have been compressed as strongly by supersonic turbulence to form an overdense sheet-like structure at parsec-scales like may have happened several parsecs away near the cloud regions that became Barnard 1 and NGC 1333. Without a comparable push to high-density that other more active regions of Perseus got, the L1451 region may have been predisposed to forming fewer stars.

9. Summary of L1451 Results

We presented observations and analysis of the L1451 region of the CARMA Large Area Star Formation Survey. We summarize the key findings below.

1. Only one compact continuum source is detected at 3 mm, down to a 3σ limit of $3.9 \text{ mJy beam}^{-1}$ ($0.08 M_{\odot}$ limit) in a $9.2'' \times 6.6''$ beam. The detected source is L1451-mm, which has previously been identified as a FHSC candidate.
2. We detect widespread HCO^+ , HCN, and N_2H^+ ($J = 1 \rightarrow 0$) emission in L1451. The HCO^+ emission covers the largest area of the cloud, which we attribute to HCO^+ tracing lower-density material than the other molecules. HCN emission morphology is nearly identical to HCO^+ , although it is weaker and less spatially extended in most regions. We detect no molecular outflows from HCO^+ or HCN. The N_2H^+ emission appears the most spatially compact, and reveals a newly identified compact core, which we call L1451-west.
3. All molecules trace gas at similar systemic velocities, but the velocity dispersion of the HCO^+ emission is significantly larger than that of HCN or N_2H^+ : mean dispersions are 0.29, 0.16, and 0.12 km s^{-1} , respectively. This is likely due to HCO^+ tracing lower-density gas at larger scales than the other two molecules; in a turbulent medium, there is more power on larger scales, which will produce larger velocity dispersions.
4. We derive column density and temperature maps from *Herschel* observations at 160, 250, 350, and 500 μm . The values were derived using modified blackbody spectrum fits to the data, and column densities agree to within 5% of *Planck* results when compared at the same angular resolution. The temperatures toward the densest regions are $\sim 2\text{--}3$ K warmer than kinetic temperatures derived from single-pointing ammonia observations toward dense cores. We attribute this difference to a limitation of using a single-component fit when modeling SEDs from cold, dense regions of molecular clouds. A simple multi-layer model shows that having warm, 17 K foreground and background emission surrounding cold, 9 K cloud emission, can cause temperatures to be overestimated by a few K, and column densities to be underestimated by a factor of two.
5. The structure of the star-forming material in L1451 that is traced by the cumulative molecular emission we detect with CLASSy is very similar to the column density structure we derived from *Herschel* observations. All of the cloud locations that are above the $A_V \sim 8$ threshold for star formation are detected in dense gas, and 90% of the molecular emission is at column densities above $1.9 \times 10^{21} \text{ cm}^{-2}$. This shows that high-resolution observations of this suite of spectral lines over large areas of molecular clouds are an excellent probe of the structure and kinematics of star forming material in young regions.
6. We use our non-binary dendrogram algorithm to identify dense gas structures in the HCO^+ , HCN, and N_2H^+ data cubes. The number of identified leaf and branch dendrogram structures decreases from HCO^+ to HCN to N_2H^+ , providing an apparently wide range of hierarchical complexity in the different tracers. However, a uniform comparison of tree statistics that accounts for differences in the noise-level of each data cube shows that all tracers are identifying structures that are fragmenting in a similar way. The differences in dendrogram branching levels and number of structures between tracers are likely due to differences in density sensitivity of the different tracers. We show that tree statistics of the gas structure surrounding L1451-mm (a confirmed young protostar or FHSC) is very similar to that of the gas surrounding Per Bolo 6 (a single-dish continuum detection), and argue this is an indication that star formation is proceeding in a similar fashion in both regions, with Per Bolo 6 a likely site of future star formation.

7. A virial analysis of dust structures identified in our *Herschel*-derived extinction map of L1451 resulted in all structures being stable against collapse when using the masses derived from single-temperature *Herschel* SED fitting and velocity dispersion from any CLASSy molecular tracer. However, we discussed how the virial parameter is likely overestimated by about a factor of two from the systematic underestimation of column densities from the simplistic single-temperature SED fitting. Also, the virial parameter of a given structure is strongly dependent on the molecular tracer used to estimate its kinetic energy; N_2H^+ and HCO^+ resulted in the lowest and highest virial parameters, respectively, with typical differences of about a factor of two. The dust structures that appear most centrally condensed in the dust maps are near or below the critical value for instability when considering the systematic uncertainty to the mass and using the N_2H^+ or HCN velocity dispersion.
8. We detect two strong, centrally condensed N_2H^+ structures: L1451-mm, and a newly identified source that we label L1451-west. L1451-mm was characterized by Pineda et al. (2011) as a FHSC candidate or young protostar. Our data shows that L1451-west is similar to, but likely younger than L1451-mm. It has strong emission from N_2H^+ but appears depleted in HCO^+ , unlike L1451-mm which has strong emission from both molecules. Both sources show N_2H^+ velocity dispersions peaking at the core center. L1451-west is less centrally condensed than L1451-mm, but more centrally condensed than the typical prestellar core; this indicates that L1451-west is likely at an evolutionary state between the typical prestellar core and a FHSC or young protostar. Follow-up observations will determine if L1451-west is a viable FHSC candidate.
9. We use our size-linewidth analysis first presented in Paper I to estimate the typical line-of-sight depth of dense gas structures in L1451. Typical inferred line-of-sight depths for HCO^+ structures are 0.40 pc, and for HCN and N_2H^+ structures are ~ 0.10 pc. These depths are found to be within a factor of two of the projected sizes of gas structures, showing that the three-dimensional dense gas morphology in L1451 is relatively ellipsoidal at the largest detectable scales when compared to the more evolved CLASSy regions that appear flattened/sheet-like at the largest scales.

Overall, these observations support the creation of complex, hierarchical dense gas structure in molecular clouds without internal feedback from protostars. We cannot say that individual structures within L1451 are definitively gravitationally bound based on our analysis, but that several structures are consistent with being unstable to collapse within the uncertainties in the data; we also know at least one star is forming in the region based on compact continuum detections. The velocities in these structures are larger than pure thermal and range from subsonic gas motions on the smallest scales (as traced by N_2H^+) to slightly supersonic gas motions on the largest scales (as traced by HCO^+); this supports external supersonic turbulence on even larger scales than those traced by HCO^+ being the driver of the first structure within the densest regions of molecular cloud complexes; those structures then become the dense, fertile grounds for the future formation of stars.

The science-ready spectral line data cubes for L1451 are hosted at our project website: <http://carma.astro.umd.edu/classy>. We welcome the community to make use of the data.

The authors would like to thank the referee for encouraging critiques that improved the paper, and all members of the CARMA staff that made these observations possible. CLASSy was supported by AST-1139990 (University of Maryland) and AST-1139950 (University of Illinois). Support for CARMA construction was derived from the Gordon and Betty Moore Foundation, the Kenneth T. and Eileen L. Norris Foundation, the James S. McDonnell Foundation, the Associates of the California Institute of Technology, the University of Chicago, the states of Illinois, California, and Maryland, and the National Science Foundation. Ongoing CARMA development and operations are supported by the National Science Foundation under a cooperative agreement, and by the CARMA partner universities.

Facility: CARMA

REFERENCES

- André, P., Di Francesco, J., Ward-Thompson, D., et al. 2014, *Protostars and Planets VI*, 27
- Aniano, G., Draine, B. T., Gordon, K. D., & Sandstrom, K. 2011, *PASP*, 123, 1218
- Ballesteros-Paredes, J. 2006, *MNRAS*, 372, 443
- Beckwith, S. V. W., & Sargent, A. I. 1991, *ApJ*, 381, 250
- Bergin, E. A., & Tafalla, M. 2007, *ARA&A*, 45, 339
- Bertoldi, F., & McKee, C. F. 1992, *ApJ*, 395, 140
- Carroll, J. J., Frank, A., Blackman, E. G., Cunningham, A. J., & Quillen, A. C. 2009, *ApJ*, 695, 1376
- Crutcher, R. M. 2012, *ARA&A*, 50, 29
- di Francesco, J., Evans, II, N. J., Caselli, P., et al. 2007, *Protostars and Planets V*, 17
- Draine, B. T. 2003, *ARA&A*, 41, 241
- Elmegreen, B. G., & Scalo, J. 2004, *ARA&A*, 42, 211
- Enoch, M. L., Evans, II, N. J., Sargent, A. I., et al. 2008, *ApJ*, 684, 1240
- Enoch, M. L., Young, K. E., Glenn, J., et al. 2006, *ApJ*, 638, 293
- Evans, II, N. J. 1999, *ARA&A*, 37, 311
- Evans, II, N. J., Dunham, M. M., Jørgensen, J. K., et al. 2009, *ApJS*, 181, 321
- Federrath, C., & Klessen, R. S. 2012, *ApJ*, 761, 156
- Federrath, C., Schrön, M., Banerjee, R., & Klessen, R. S. 2014, *ApJ*, 790, 128
- Fernández-López, M., Arce, H. G., Looney, L., et al. 2014, *ApJ*, 790, L19
- Galliano, F., Hony, S., Bernard, J.-P., et al. 2011, *A&A*, 536, A88
- Hatchell, J., Richer, J. S., Fuller, G. A., et al. 2005, *A&A*, 440, 151
- Johnstone, D., Di Francesco, J., & Kirk, H. 2004, *ApJ*, 611, L45
- Jørgensen, J. K., Johnstone, D., Kirk, H., et al. 2008, *ApJ*, 683, 822
- Kauffmann, J., Bertoldi, F., Bourke, T. L., Evans, II, N. J., & Lee, C. W. 2008, *A&A*, 487, 993
- Kauffmann, J., Pillai, T., & Goldsmith, P. F. 2013, *ApJ*, 779, 185
- Kirk, H., Johnstone, D., & Di Francesco, J. 2006, *ApJ*, 646, 1009
- Klessen, R. S., & Hennebelle, P. 2010, *A&A*, 520, A17
- Larson, R. B. 1981, *MNRAS*, 194, 809
- Lee, K. I., Fernández-López, M., Storm, S., et al. 2014, *ApJ*, 797, 76
- McKee, C. F., & Ostriker, E. C. 2007, *ARA&A*, 45, 565

- McKee, C. F., & Zweibel, E. G. 1992, *ApJ*, 399, 551
- Meisner, A. M., & Finkbeiner, D. P. 2015, *ApJ*, 798, 88
- Nakamura, F., & Li, Z.-Y. 2007, *ApJ*, 662, 395
- . 2014, 783, 115
- Pineda, J. E., Arce, H. G., Schnee, S., et al. 2011, *ApJ*, 743, 201
- Planck Collaboration, Abergel, A., Ade, P. A. R., et al. 2014, *A&A*, 571, A11
- Prasad, S. S., & Huntress, Jr., W. T. 1980, *ApJS*, 43, 1
- Rosolowsky, E. W., Pineda, J. E., Foster, J. B., et al. 2008a, *ApJS*, 175, 509
- Rosolowsky, E. W., Pineda, J. E., Kauffmann, J., & Goodman, A. A. 2008b, *ApJ*, 679, 1338
- Sadavoy, S. I., di Francesco, J., André, P., et al. 2012, *A&A*, 540, A10
- Sault, R. J., Teuben, P. J., & Wright, M. C. H. 1995, in *Astronomical Society of the Pacific Conference Series*, Vol. 77, *Astronomical Data Analysis Software and Systems IV*, ed. R. A. Shaw, H. E. Payne, & J. J. E. Hayes, 433
- Shetty, R., Kauffmann, J., Schnee, S., Goodman, A. A., & Ercolano, B. 2009, *ApJ*, 696, 2234
- Shirley, Y. L. 2015, *PASP*, 127, 299
- Storm, S., Mundy, L. G., Fernández-López, M., et al. 2014, *ApJ*, 794, 165
- van der Tak, F. F. S., Black, J. H., Schöier, F. L., Jansen, D. J., & van Dishoeck, E. F. 2007, *A&A*, 468, 627
- Williams, J. P., de Geus, E. J., & Blitz, L. 1994, *ApJ*, 428, 693

A. Noise Dependence of Dendrogram Structure and Statistics

In Paper I, we analyzed a single non-binary dendrogram from the position-position-velocity (PPV) cube of the isolated hyperfine component of N_2H^+ in Barnard 1. In this paper, we analyzed the non-binary dendrograms from the PPV cubes of the strongest hyperfine components of N_2H^+ and HCN , and the single component of HCO^+ in L1451. There was a noise difference of 15% between those cubes, and the goal of this section is to establish how we can compare dendrogram structure and statistics of data with different noise-levels. We will argue that the key for a proper comparison is to construct the dendrograms using absolute, physical units (as opposed to units based on the sensitivity of an individual data set) for certain dendrogram algorithm parameters, including the parameters for: 1) the minimum height for a local maximum to peak above the level where it merges with adjacent local maxima to be considered a real leaf (`minheight`), and 2) the minimum allowed branching step height between adjacent levels in the dendrogram (`stepsize`).

We will demonstrate those points using two integrated intensity maps of Barnard 1⁴ that have similar signal but different noise, created from different hyperfine components in the N_2H^+ PPV cube presented in

This preprint was prepared with the AAS L^AT_EX macros v5.2.

⁴We use Barnard 1 instead of L1451 for demonstration in this appendix because Barnard 1 was the first CLASSy region analyzed and used to test the dendrogram analysis methods.

Paper I. The N_2H^+ ($J = 1 \rightarrow 0$) transition is split into seven resolvable hyperfine components, which have effectively the same velocity dispersion and excitation condition but different peak intensity. We can integrate over different combinations of hyperfine components to create moment maps with different signal-to-noise ratio (SNR). Specifically, we integrate over all seven hyperfine components to create a “full-velocity component” integrated intensity map (referred to as the FVC map later in the section), and over the isolated velocity component to make the “lowest-velocity component” integrated intensity map (referred to as the LVC map later in the section). The LVC map has lower signal than the FVC map, but also lower noise (σ_{LVC}) in emission-free regions compared to the FVC map (σ_{FVC}), since noise scales as $\sqrt{N}\sigma$, where N is the number of channels, and σ is the noise in a single channel.

The questions we want to answer hinge on how to consistently analyze dendrogram structure and statistics when we change the noise in a map while keeping the signal the same. Therefore, we normalize the FVC map to have the same signal as the LVC map in regions where the LVC map has emission greater than $6\sigma_{LVC}$. In regions less than $6\sigma_{LVC}$ in the LVC map, we scale the FVC map down by a factor of 7, which is the mean normalization factor in regions of strong signal. We then calculate the rms of the normalized FVC map (referred to as the NFVC map later in the section), σ_{NFVC} , which is $0.03 \text{ Jy beam}^{-1} \text{ km s}^{-1}$, compared to σ_{LVC} of $0.09 \text{ Jy beam}^{-1} \text{ km s}^{-1}$. The result is a NFVC map with similar signal to the LVC map with three times lower noise; this is the scenario we want to test our dendrogram algorithm on.

We ran our non-binary dendrogram algorithm on the Barnard 1 versions of these two maps in two different ways. First, we allowed each dendrogram to have a `stepsize` and `minheight` based on the rms of each map, meaning `stepsize` = $1\sigma_{NFVC}$ and `minheight` = $2\sigma_{NFVC}$ for the NFVC map, and `stepsize` = $1\sigma_{LVC}$ and `minheight` = $2\sigma_{LVC}$ for the LVC map. Second, we forced each dendrogram to have the same `stepsize` and `minheight` based on the noisier map, meaning `stepsize` = $1\sigma_{LVC}$ and `minheight` = $2\sigma_{LVC}$ for both maps. Using absolute units across maps as in this second case could be beneficial because absolute units are linked with physical properties of a cloud, while noise units are linked with the properties of the individual observations. For example, if a study wants to link fragmentation properties of column density structure in different clouds to the properties of star formation in those clouds, it would be more sensible to define an absolute unit, such as a minimum mass or column density that is always the same across clouds, for branching and leaf identification, rather than a noise unit, such as 1σ , which can be different for different clouds.

For the first case, where we allowed the `stepsize` and `minheight` parameters to be based on the noise-level of the individual map, the resulting dendrogram-identified structures for the two Barnard 1 maps are shown in Figure 21, and the dendrograms are shown in Figure 22. Two of the strongest peaks in the region are similarly identified in both maps (structures 9 and 11 in the LVC map are 27 and 31 in the NFVC map). However, some leaves break up into multiple structures when lowering the noise of the map and also lowering the absolute threshold for creating a leaf and a branching step (structure 6 in the LVC map becomes structures 22, 23, 25, and 28 in the NFVC map).

This shows that the hierarchical structure of two maps of the same region that have different noise can significantly change if `minheight` and `stepsize` are kept in terms of the sensitivity of each individual map. This makes sense if we consider an extreme limit of very low noise maps that may soon be produced by ALMA. If the noise in a map is extremely reduced, structures peaking 2σ above a merger level with other structures would likely not represent physically relevant features, but small-scale variations on top of physical meaningful features. In this case of extremely low noise, it would make more sense to define a physically relevant minimum unit for studying structure, such as a minimum mass.

For the second case, we used the values of the LVC map for `stepsize` and `minheight` for the construction of both dendrograms. That meant that each dendrogram could branch in $0.09 \text{ Jy beam}^{-1}$ steps, and leaves needed to be $0.18 \text{ Jy beam}^{-1}$ above their merge level to be considered real—these were our minimum physically relevant units to study structure across these two maps with different noise. The resulting dendrogram-identified structures for the two Barnard 1 maps are shown in Figure 23, and the dendrograms are shown in Figure 24.

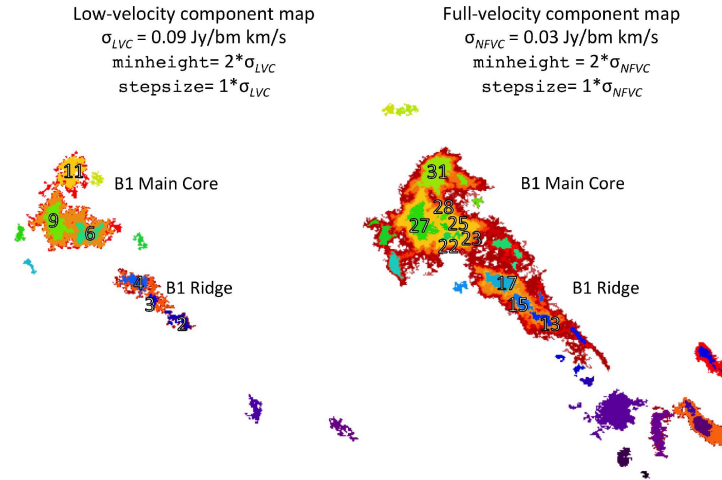


Fig. 21.— Structures identified by our non-binary dendrogram algorithm from the Barnard 1 integrated intensity maps made from the lowest-velocity hyperfine component (left) and from all hyperfine components normalized as discussed in the text (right). The dendrogram algorithm parameters are listed in the figure, and are based on the noise level of the individual maps. Structures are labeled with numbers that correspond to leaves and branches in Figure 22. See Paper I for a description and analysis of the Barnard 1 region.

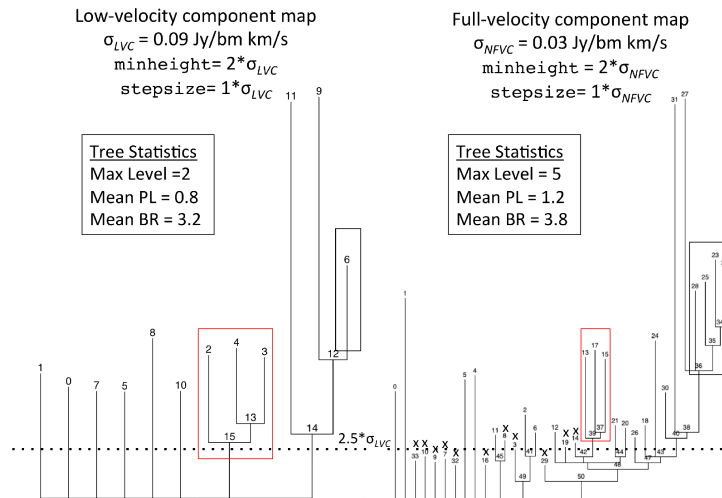


Fig. 22.— Non-binary dendrograms from the integrated intensity maps made from the lowest-velocity hyperfine component (left) and from all hyperfine components normalized as discussed in the text (right) using the dendrogram algorithm parameters listed in the figure. The boxes highlight examples of the same regions of emission between the two maps for a comparison of identified structures when using non-uniform algorithm parameters on maps with different noise levels. The tree statistics in the figure inset are discussed in the text. See Paper I for a description and analysis of the Barnard 1 region.

The main take-away from these figures is that lowering the noise but keeping the same absolute units for studying structure results in very similar dendrograms. A large-scale, low-intensity branch (structure 16 in the NFVC map) is added around smaller-scale, higher-intensity structures found in the LVC map, and some leaves that branched directly from the tree base in the LVC map now branch from one level up due to the addition of the large-scale, low-intensity branch (e.g., leaf 8 becomes leaf 7). The strongest peaks in the region are similarly identified in both maps (structures 6, 9, and 11 in the LVC map are 6, 8, 10 in the NFVC map); lowering the noise did not cause these structures to break up. This provides evidence that if the noise in a map is lowered, and the `stepsize` and `minheight` parameters are kept constant, the hierarchical structure will not significantly

change—the main effect is to add lower-intensity branching structure to connect parts of the emission hierarchy not previously connected.

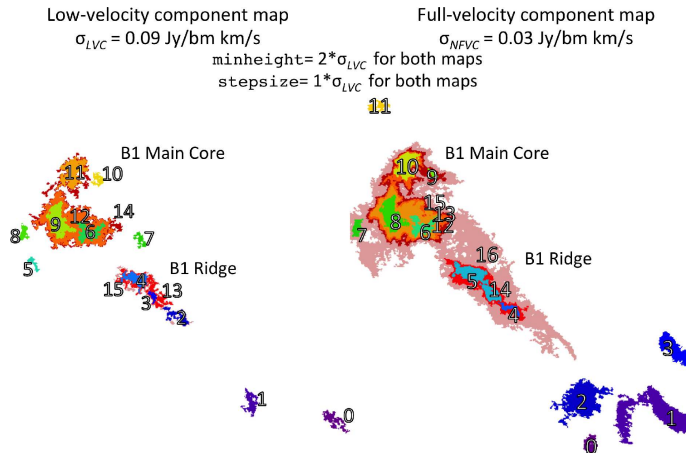


Fig. 23.— Structures identified by our non-binary dendrogram algorithm from the Barnard 1 integrated intensity maps made from the lowest-velocity hyperfine component (left) and from all hyperfine components normalized as discussed in the text (right). The dendrogram algorithm parameters are listed in the figure, and are the same for each map. Structures are labeled with numbers that correspond to leaves and branches in Figure 24. See Paper I for a description and analysis of the Barnard 1 region.

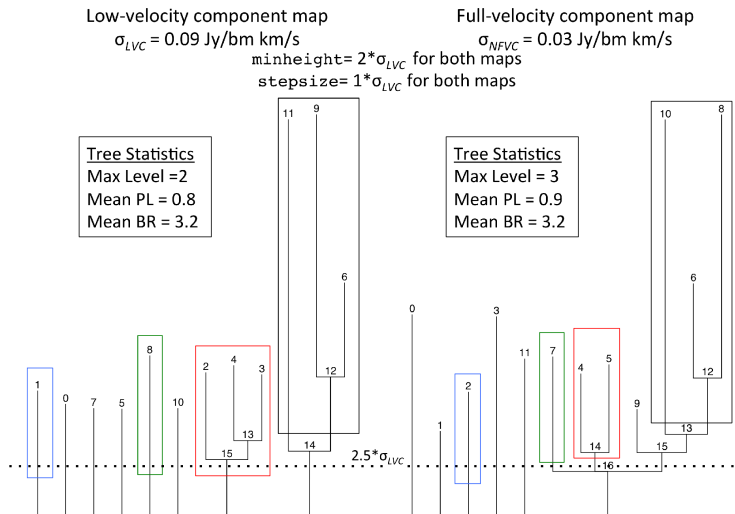


Fig. 24.— Non-binary dendrograms from the integrated intensity maps made from the lowest-velocity hyperfine component (left) and from all hyperfine components normalized as discussed in the text (right) using the uniform dendrogram algorithm parameters listed in the figure. The colored boxes highlight examples of the same regions of emission between the two maps for a comparison of identified structures when using uniform algorithm parameters on maps with different noise levels. The tree statistics in the figure inset are discussed in the text. See Paper I for a description and analysis of the Barnard 1 region.

Another important test is how the tree statistics change between the dendrograms when the noise changes. We calculate the tree statistics of the LVC map in both cases as described in Paper I, and list the statistics as insets of Figures 22 and 24. To compare statistics between the LVC and NFVC maps in each case, we only consider the dendrogram structures in the NFVC map above the mask level applied to the LVC map. The dendrogram of the LVC map has a minimum integrated intensity of $0.21 \text{ Jy beam}^{-1} \text{ km s}^{-1}$ (set by the $2.5\sigma_{LVC}$ mask limit to the data input to the dendrogram algorithm). Since the NFVC map extends to lower emission

levels set by a $2.5\sigma_{NFVC}$ mask limit, we calculate the statistics for that dendrogram above a cut corresponding to the same $2.5\sigma_{LVC}$ limit of the LVC map (the cut is represented in Figures 22 and 24 by the horizontal dashed line). This means that leaves from the NFVC map must peak $2\sigma_{NFVC}$ or $2\sigma_{LVC}$ above the noisier mask level to be considered real, for the first and second case, respectively. The leaves that do not meet this requirement are marked with an “x” in Figures 22 and 24. Any branch below this noisier mask level is removed, and structures above it are lowered one level.

For the first case, where we set `stepsize` and `minheight` based on the noise-level of the individual map, the NFVC dendrogram has a maximum branching level three levels higher than the LVC dendrogram, a mean path length about half a level larger than the LVC dendrogram, and a mean branching ratio 0.6 higher than the LVC dendrogram. The differences in maximum branching level and mean path length can be explained by the NFVC map having a lower absolute threshold for what can be considered a leaf compared to the LVC map (`minheight` of $0.06 \text{ Jy beam}^{-1} \text{ km s}^{-1}$ vs. $0.18 \text{ Jy beam}^{-1} \text{ km s}^{-1}$), and allowing branching steps at smaller absolute units compared to the LVC map (`stepsize` of $0.03 \text{ Jy beam}^{-1} \text{ km s}^{-1}$ vs. $0.09 \text{ Jy beam}^{-1} \text{ km s}^{-1}$); when it is easier to break emission into leaves and to define new branching levels, there will be more hierarchical structure in the dendrogram.

For the second case, where we set `stepsize` and `minheight` based on a minimum relevant $\text{Jy beam}^{-1} \text{ km s}^{-1}$ value, the mean path lengths agree to a tenth of a level, the mean branching ratios are identical, and the maximum branching levels differ by only one level. This demonstrates how tree structure can be defined so that lowering the noise of a map will not alter the calculated tree statistics significantly. When comparing different clouds with different noise-levels, it will be important to use a minimum relevant value for algorithm parameters so that the emission in each cloud has the same absolute threshold for what can be considered a leaf and what can be considered a significant branching step.

In conclusion, the dendrograms of clouds observed with different noise can be uniformly compared if the comparison uses absolute units for the dendrogram contouring and leaf requirements instead of units based on the noise-level of each individual map, and if the comparison of tree statistics only analyzes structures above a minimum intensity level set by the noisiest map.